Eveline KUHNERT, B.Sc.

Negating the Interfacial Resistance in Composite Electrolytes for Advanced Li-ion Batteries

MASTER'S THESIS

to achieve the university degree of

Diplom-Ingenieurin

Master's degree programme:

Technical Chemistry

submitted to

Graz University of Technology

Supervisors:

Univ.-Prof. Dr. habil. Martin Wilkening

Priv.-Doz. Mag. Dr. Daniel Rettenwander

Institute for Chemistry and Technology of Materials

Graz, January 2021

EIDESSTATTLICHE ERKLÄRUNG
AFFIDAVIT

Ich erkläre an Eides statt, dass ich die vorliegende Arbeit selbstständig verfasst, andere als die angegebenen Quellen/Hilfsmittel nicht benutzt, und die den benutzten Quellen wörtlich und inhaltlich entnommenen Stellen als solche kenntlich gemacht habe. Das in TUGRAZonline hochgeladene Textdokument ist mit der vorliegenden Masterarbeit identisch.

I declare that I have authored this thesis independently, that I have not used other than the declared sources/resources, and that I have explicitly indicated all material which has been quoted either literally or by content from the sources used. The text document uploaded to TUGRAZonline is identical to the present master's thesis.

_____ _____

Datum / Date Unterschrift / Signature

ABSTRACT

Compared to Lithium-ion batteries with liquid electrolytes, all-solid-state batteries (ASSBs) based on solid composite electrolytes (SCEs) offer improved safety, energy density and power. SCEs consist of an inorganic filler, incorporated in a polymeric matrix, and integrate the advantages of ceramic- and polymer electrolytes. Ceramic electrolytes (CEs) possess high Li-ion conductivity and electrochemical stability, but their application is limited due to brittleness and the poor interfacial contact between the electrolyte and the electrode material. In SCEs the beneficial properties of flexible polymers and high-ion-conducting CEs are combined. Despite extensive research effort, the development of this technology is still hindered, as long as the high interfacial resistance across the ceramic|polymer interface poses a severe problem.

Herein, a new surface modification strategy is introduced to negate the interfacial resistance in SCEs, comprising of garnet-structured $Li_{6.4}Ga_{0.2}La_3Zr_2O_{12}$ (Ga-LLZO) and poly(ethylene oxide) (PEO). Furthermore, the effect of a plasticizer (Oxa-Michael Product, OMP) on the Li-ion conducting properties of PEO is investigated and advanced SCEs are made. The thermal behavior, crystallinity, structure, phase composition, and ionic conductivity of the composites are investigated by using X-ray powder diffraction (XRD), nuclear magnetic resonance spectroscopy (NMR), differential scanning calorimetry (DSC) and electrochemical impedance spectroscopy (EIS). In a first step, the compositional dependence of the Li-ion conductivity is observed by varying the Ga-LLZO content in the PEO matrix. The highest Li-ion conductivity of 9.0×10^{-6} S cm^{-1} at RT is obtained in PEO:Ga-LLZO composites containing a fraction of 30 wt.% Ga-LLZO. In a second step, the contribution of LLZO grain boundaries to the electrolyte resistance is observed via EIS analysis of surface modified LLZTO|PEO bilayer cells. Therefore, the surface-terminated oxygen of the LLZTO is activated by plasma etching and functionalized with a solution of (3-glycidyloxypropyl)trimethoxysilane (Si-R) to form covalently bonded Si-R layers. The Si-R layers are terminated by an epoxy group, that reacts with the hydroxyl group of the PEO via a ring-opening reaction. As a result, the free volume between LLZTO and PEO is decreased, and a fast charge transfer across the interface is provided. An interface resistance of 500 Ω cm^2 at 20 °C is achieved, which is among the lowest values reported so far. In a last step, composites of modified Ga-LLZO particles and PEO are made. To further increase the Li-ion conducting properties of the SCEs, OMP is added as a plasticizer to the polymer matrix. A significant improvement of the Li-ion conductivity to a value of 8.3×10^{-5} S cm^{-1} at RT in advanced SCEs is achieved, which makes them a promising electrolyte for the next generation of all-solid-state Li-ion batteries.

KURZFASSUNG

Im Vergleich zu herkömmlichen Lithium-Ionen Batterien mit einem Flüssigelektrolyten, weisen Festkörperbatterien auf Basis von Kompositelektrolyten eine erhöhte Energie- und Leistungsdichte, sowie ein wesentlich geringeres Sicherheitsrisiko auf. Kompositelektrolyte bestehen aus einem anorganischen Füllstoff in einer Polymermatrix und kombinieren die vorteilhaften Eigenschaften von Festkörper- und Polymerelektrolyten. Keramik basierte Festkörperelektrolyte erzielen hohe Leitfähigkeiten und elektrochemische Stabilität, der schlechte Grenzflächenkontakt und die Sprödigkeit dieser Materialien limitieren jedoch ihre Anwendung. In Kombination mit flexiblen Polymeren können die anwendungsrelevanten Eigenschaften der beiden Materialien vereint, und vielversprechende Verbundmaterialien hergestellt werden. Die Realisierung solcher Systeme ist derzeit jedoch noch mit großen Herausforderungen, wie dem hohen Grenzflächenwiderstand zwischen Keramik und Polymer verbunden.

Die hier vorliegende Arbeit befasst sich mit der Reduktion des Grenzflächenwiderstands durch die Oberflächenmodifikation von $Li_{6.4}Ga_{0.2}La_3Zr_2O_{12}$ (Ga-LLZO) Partikeln in Polyethylenoxid (PEO):Ga-LLZO basierten Kompositelektrolyten. Desweiteren wird ein Weichmacher (Oxa-Michael Produkt, OMP) in die PEO-Matrix inkorporiert, und dessen Auswirkungen auf die Li-Ionen Leitfähigkeit in fortgeschrittenen Verbundmaterialien untersucht. Mittels Röntgendiffraktion (X-ray diffraction, XRD), Kernspinresonanzspektroskopie (Nuclear magnetic resonance spectroscopy, NMR), Differentialthermoanalyse (Differential scanning calorimetry, DSC) und elektrochemischer Impedanzspektroskopie (EIS) werden die Temperaturabhängigkeit, die Kristallinität, die Struktur, die Phasenzusammensetzung und die ionische Leitfähigkeit der Elektrolyte ermittelt. In einem ersten Schritt wird die Abhängigkeit der Li-Ionen-Leitfähigkeit vom Verhältnis von PEO zu Ga-LLZO in den Kompositen durch Variation des Ga-LLZO-Gehalts in der PEO-Matrix untersucht. Die höchste Li-Ionen-Leitfähigkeit von $9{,}0 \times 10^{-6}$ S cm^{-1} bei RT wird in PEO:Ga-LLZO Membranen mit einem Anteil von 30 wt.% Ga-LLZO erhalten. In einem zweiten Schritt wird der Beitrag der LLZO-Grenzfläche zum Elektrolytwiderstand durch die EIS-Analyse oberflächenmodifizierter LLZTO|PEO-Doppelschichtzellen untersucht. Dazu wird der Oberflächen-terminierte Sauerstoff des LLZTO durch Plasmaätzen aktiviert, und mit einer Lösung aus (3-Glycidyloxypropyl)trimethoxysilan (Si-R) zu kovalent gebundenen Si-R-Schichten funktionalisiert. Die Si-R-Schichten besitzen Epoxid-Endgruppen, welche mit den Hydroxylgruppen des PEO in einer Ringöffnungsreaktion reagieren. Dadurch wird das freie Volumen zwischen LLZTO und PEO verringert und eine schnelle Ladungsübertragung über die

Grenzfläche ermöglicht. Ein Grenzflächenwiderstand von 500 Ω cm^2 bei 20 °C wird erreicht, was im Bereich der niedrigsten Werte liegt, welche aus der Literatur bekannt sind. In einem letzten Schritt werden Kompositmembranen aus modifizierten Ga-LLZO-Partikeln und PEO hergestellt. Um die Li-Ionen-leitenden Eigenschaften der Verbundmaterialien weiter zu erhöhen, wird OMP als Weichmacher zu der Polymermatrix hinzugefügt. Eine deutliche Verbesserung der Li-Ionen-Leitfähigkeit auf einen Wert von $8{,}3 \times 10^{-5}$ S cm^{-1} bei RT wird erreicht, was diese Elektrolyte zu vielversprechenden Materialien für die nächste Generation von Festkörperbatterien macht.

VORWORT

I am grateful to Univ.-Prof. Dr. habil. Martin Wilkening for giving me the opportunity to perform my master thesis at the Institute of Chemistry and Technology of Materials (TU Graz, Austria). Special thanks is to my university advisor Priv.-Doz. Mag. Dr. Daniel Rettenwander for his consistent support whenever needed. The door to his office was always open whenever I had a question about my research or writing. Thank you Daniel for the excellent guidance. Futhermore, I would like to thank the whole Wilkening working group and all other collegues on the institute, especially Assoc. Prof. DI Dr. Christian Slugovc, Univ.-Prof. Dr. Gregor Trimmel, DI. Dr. Thomas Rath for their scientific expertise and technical support.

Support by the Austrian Federal Ministry for Digital and Economic Affairs, the National Foundation for Research, Technology and Development, the Christian Doppler Research Association (Christian Doppler Laboratory for Solid-State Batteries) and the Austrian Science Fund (FWF) (project no. P25702) is gratefully acknowledged.

Last but not least; I am deeply grateful to my family and friends, especially my parents for their love and exceptional support along this journey of learning and personal development.

Graz, January 2021

Evi

LIST OF ABBREVATIONS

AC	Alternating Current
ASSBs	All-solid-state Batteries
ASSLIBs	All-solid-state Li-ion Batteries
CEs	Ceramic Electrolytes
CPE	Constant Phase Element
EC	Ethylene Carbonate
EIS	Electrochemical Impedance Spectroscopy
EV	Electronic Vehicle
E(t)	Sinusoidal potential Excitation
eV	Electron Volt
Ga-LLZO	Gallium-Lithium-Lanthanum-Zirconate
GHz	Gigahertz
Hz	Hertz
I(t)	Current
$LiAsF_6$	Lithium hexafluoroarsenate
LiB_4	Lithium tetrafluoroborate
$LiClO_4$	Lithium perchlorate
$LiPF_6$	Lithium hexafluorosphate
Li_6PS_5Cl	Lithium thio-phosphates
LISICON	Lithium Super Ionic Conductors
LiTFSI	Lithium bis(trifluoromethanesulfonyl) imide
LLTO	Lithium-Lanthanum-Titanate
LLZO	Lithium-Lanthanum-Zirconate
LLZTO	Lithium-Lanthanum-Zirconium-Tantalum-Oxide
MHz	Megahertz
NASICON	Sodium Super Ionic Conductors
NMR	Nuclear Magnetic Resonance
OH	Hydroxy groups
OMP	Oxa-Michael Product
PC	Propylene Carbonate
PEO	Polyethylene oxide
SCEs	Solid Composite Electrolytes
SEI	Solid Electrolyte Interface
Si-R	(3-glycidyloxypropyl)trimethoxysilane
SN	Succinonitrile
SPEs	Solid Polymer Electrolytes
U(t)	Voltage
VTF	Vogel-Tammann-Fulcher
wt.%	Weight percent
XRD	X-ray Diffraction

LIST OF FIGURES

CONTENTS

1 INTRODUCTION

Lithium-ion batteries are currently the most efficient, rechargeable energy storage and power sources. With their long cycle life, high energy densities (up to 260 Wh kg^{-1})[1] and potential for yet higher capacities, they are used in high-end electronics and have recently entered the power tool and electronic vehicle (EV) market.[2] The world's growing energy demand encourages the battery development to continue, and in the past few years there have been significant changes in the traditional aqueous electrolyte-based Li-ion battery system. One approach to increase the energy density is to use a lithium metal anode, providing both: high voltage and excellent capacity.[3] The major obstacle in this setup is arising from the reactivity of the electronegative metal. The poor rechargeability can lead to dendrite formation on the lithium electrode which may cause serious safety concerns like fires and explosion hazards. All-solid-state Li-ion batteries (ASSLIBs) provide a liquid-free solution and overcome safety concerns of the conventional solvent based battery systems.

In general solid-state electrolytes (SSEs) can be divided into solid polymer electrolytes (SPEs), ceramic electrolytes (CEs), and solid composite electrolytes (SCEs).[4] Selecting a solid electrolyte goes hand-in-hand with a compromise between high Li-ion conductivity, stability and the ease of fabrication.[5] SPEs are being investigated as promising candidates to replace liquid electrolytes because of their flexibility, good interfacial contact and low processing costs. CEs on the contrary benefit from a high ionic conductivity (10^{-3} to 10^{-2} S cm^{-1})[4], good electrochemical and thermal stability and high mechanical strength. SCEs combine the beneficial properties of both – SPEs and CEs. High ionic conductivities > 10^{-3} S cm^{-1} can be reached and the challenge of interfacial contact with the electrodes is addressed. Still, the introduction of composite electrolytes comes along with some fundamental challenges. The high interfacial resistance of ion transport across the ceramic|polymer interface leads to an increased internal impedance and a reduced cycle life.

The structure of this thesis is as follows: in the remainder of this chapter, some basic theory about ASSLIBs and different SSEs is outlined. Their characteristics are introduced, and the interfacial transport mechanisms are discussed. Further, the main measurement methods X-ray Diffraction (XRD) and Electrochemical Impedance Spectroscopy (EIS) are explained. In the second chapter "Materials Characterization", the used analysis techniques are briefly outlined. The experimental part includes information about the material synthesis, the electrolyte preparation and further measurement details. In the chapter "Results and Discussion", the measurement results are shown and the findings of this thesis work are discussed.

2 THEORETICAL ASPECTS

2.1 All-Solid-State Li-ion Batteries (ASSLIBs)

Basically, conventional Li-ion batteries consist of an anode, a liquid electrolyte (LE), a separator, and a cathode. The LE solutions are generally made up of a lithium salt such as Lithium hexafluorophosphate ($LiPF_6$) or Lithium bis(trifluoromethanesulfonyl) imide (LiTFSI) and an organic solvent. The use of organic electrolyte solutions gives rise to safety issues associated with potential electrolyte leakage and inherent flammability. If exposed to extreme conditions of elevated voltage and temperature, these electrolytes can react with the active electrode materials to release significant heat and gas.[6]

In order to overcome the safety issues related to the use of LEs in conventional LIBs, a number of solid electrolyte alternatives have been explored in ASSLIBs. SSEs are typically less reactive than LEs, and can provide high chemical and thermal stability and electrochemical inertness in a wide potential window. Furthermore, the change in materials allows the use of lithium metal as an anode material by reducing the risk of shortcircuiting due to lithium dendrite growth, resulting in a large increase in the energy density of the battery. In addition, SSEs can act as rigid physical barriers between the anode and cathode, enabling a bipolar electrode configuration which is advantegeaus for optimizing energy density and space utilisation.[7] The structural differences of commercial liquid-based and ASSLIBs are represented in Figure 1. In ASSLIBs the anode and cathode are separated by a thin SSE, whereas the conventional liquid-based LIB system makes use of a liquid electrolyte solution to regulate the flow of current.

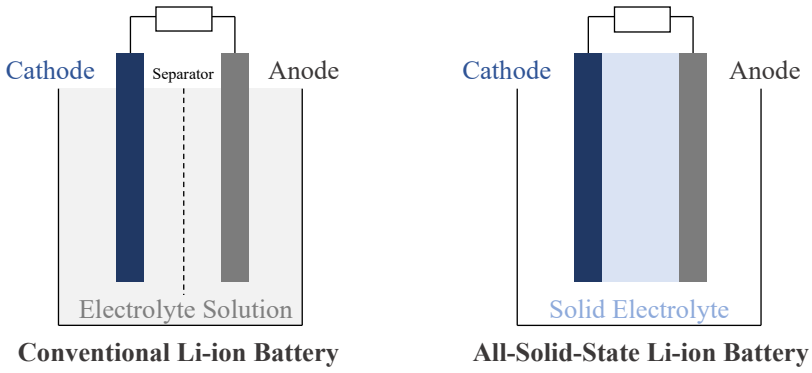

Figure 1. Schematic illustration of LIBs with liquid- and solid-state electrolyte.

Despite several advantages, the replacement of a liquid electrolyte by a solid electrolyte is still in an early research state. The key limiting factor for the implementation of SSEs in the battery field

is ascribed to a high internal resistance for Li-ion transfer over the solid-solid electrode-electrolyte interfaces, negatively affecting electrochemical performance of the cell and reducing cycle life. Unlike LEs, SSEs cannot form an intimate contact with the cathode or anode interfaces, resulting in interfacial complications between the electrolyte and the electrode material. The poor wettability of SSEs with other components results in a high charge-transfer resistance, and thus the rapid deterioration of ASSB performance. Therefore, the design of highly conductive SSEs should not only consider the chemical and electrochemical stabilities, but also the interfacial mechano-electrochemistry.[7] In order for SSEs to replace the current LEs, advanced materials are required for optimum performance of the battery system.

2.2 Solid-State Electrolytes (SSEs)

A large variety of materials can be used as solid-state electrolytes. The three main categories include ceramic electrolytes (CEs), solid polymer electrolytes (SPEs), and solid composite electrolytes (SCEs).[4] For their application in LIBs several essential requirements have to be fulfilled such as high Li-ion conductivity and chemical and thermal stability. Currently, among the most promising candidates to be used as solid electrolytes in ASSLIBs are thio-phosphates (e.g., crystalline Li_6PS_5Cl)[8,9], oxides (e.g., garnet-type $Li_7La_3Zr_2O_{12}$ (LLZO))[10,11] and polymers (e.g., polyethylene oxide (PEO)).[5,12] Solid composite electrolytes based on a combination of two different solid electrolyte systems (e.g. PEO:LLZO) benefit from the merits of the different components.

2.2.1 Solid Composite Electrolytes (SCEs)

To enhance the ionic conductivity and mechanical properties of SPEs, inorganic fillers are often introduced into the polymer matrix. With the combined effect of polymer and inorganic filler, the conductivity and mechanical strength as well as the interface stability can be greatly improved in SCEs. The key functionalities of the introduction of inorganic fillers mainly relay on three aspects: i) crystallinity reduction, ii) electrode-electrolyte interfacial stability enhancement, and iii) cation transference number improvement.[13] The incorporation of cost-effective polymers on the other hand significantly improves the flexibility and process ability of the SCEs.

In order to further improve the room-temperature ionic conductivity, plasticizers can be added to the electrolyte system. Partial substitution of a high-molecular weight polymer with a lower-

molecular weight polymer leads to a reduction of crystallinity and increases the free volume of the system.[14] The main aspects that restrict the electrochemical performance of SCEs are related to the ionic conduction processes across the ceramic|polymer interphase.

2.2.1.a.1 Ionic Transport across the Ga-LLZO|PEO Interface

In single-component ion conductors the ionic conductivity is attributed to the transport pathways and the concentration and mobility of ions. The conduction of ions in SCEs is more complex as there are multiple phases involved in the transport processes. Various studies observed a compositional dependence of the Li-ion transport in the polymer-ceramic electrolytes.[15,16] Li et al. (2019)[16] showed, that the Ga-LLZO-content in Ga-LLZO:PEO composites has a significant influence on the conductivity. At a concentration below 4 vol % the total conductivity of the Ga-LLZO:PEO composite stays at a low value. The conductivity continuously increases between 4 to 16 vol % of LLZO fraction, at which the composite shows a maximum conductivity value. With further increase of the Ga-LLZO content, the nanoparticles start to aggregate, resulting in a disruption of the Li-ion conducting pathways and furthermore in a decrease of conductivity.[16] Depending on the composition of the composite and the interfaces, the Li-ion transport can take place by one or more different mechanisms. The interface resistance between the ceramic particles and the PEO matrix influences the Li-ion transport in the SCEs. Figure 2 indicates the Li-ion movement in a composite with high interfacial resistance (a) where the Li-ions may move through the bulk phase whereas the Li-ions in a composite with low interface resistance (b) can move across the interface and through the ceramic phase, providing a much faster conduction process.

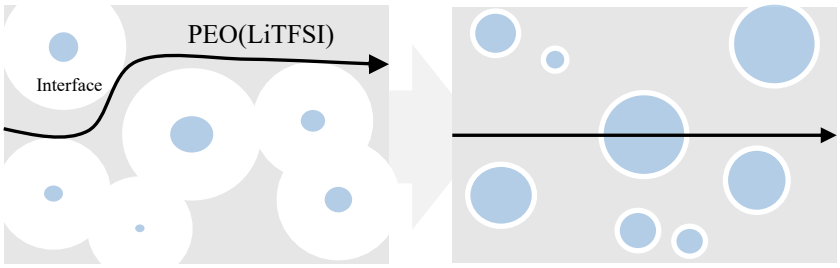

Figure 2. Schematic of the Li-ion pathways (black arrows) in SCEs. In (a) the Li-ions only move through the bulk phase because of the high interfacial resistance between LLZO and PEO. In a composite with low interfacial resistance between LLZO and PEO (b) the Li-ion conduction across the interface and through the ceramic phase is possible.

The incompatible interface wetting behavior in (a) results in a huge interfacial resistance between the ceramic nanoparticles and the polymeric matrix. Hence, it is of great interest to minimize the interfacial resistance in SCEs to enable the Li-ion transport through the ceramic phase.

2.2.1.a.2 Covalent Surface Modification of Ceramic Surfaces

A substantial improvement of the interfacial resistance in composite electrolytes can be achieved by modifying the ceramic oxide surface.[17] The reactivity of the surface-bound oxygen groups enables the covalent attachment of monolayers. Among the various possibilities to obtain surface activation, plasma etching, dry- and wet-etching are the main methods used on a lab scale.[17] Six major attachment chemistries exist that have been used to covalently bind organic monolayers onto oxides (silanes, phosphonates, carboxylates, catechols, alkenes/alkynes and amines).[17] One of the most common methods is to use alkylsilanes for the functionalization. The covalent linkage between the substrate and the OH-anchoring group is rapidly formed and stabilizes the monolayer.[18] A schematic representation of the formation of covalently bonded monolayers on plasma-activated LLZTO is shown in Figure 3.

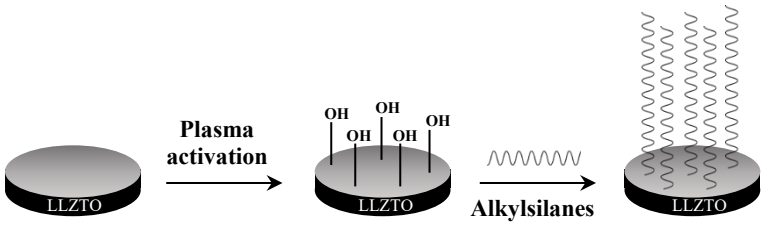

Figure 3. Schematic of the formation of covalent bonds on plasma-activated LLZTO.

There are two attachment methods available for the surface modification with silanes: reactions in solution or in the vapor phase.[17] Silane monolayer formation from solution was first reported by Sagiv (1978)[19]. Since then various Alkylsilanes like $RSiX_3$, R_2SiX_2, or R_3SiX, (where R is an alkyl group and X is a leaving group, such as chloride, alkoxy, or hydride) have been introduced for the reaction with OH-bearing surfaces.[17] Among those, 3-Glycidyloxypropyl)trimethoxysilane (Si-R) can be used to prepare epoxy-functionalized silica nanoparticles. The epoxy ring, positioned at the end of the Si-R molecule, reacts easily with the PEO-OH group by a ring-opening reaction and acts as linking agent between the surface of the silica and the polymeric matrix.[20,21] This reaction supports the ordered arrangment of PEO segments around the ceramic particles and improves the Li-ion transport across the ceramic|polymer interphase.[5]

The effectiveness of silane modification is highly dependent on the surface chemistry of the inorganic substrate. Excellent substrates for silane modification are surfaces containing Si-OH surface groups such as silica, but ceramic oxide surfaces can also be treated to form strong

interfacial bonds.[17,22] The silane surface treatment of garnet-type oxide $Li_7La_3Zr_2O_{12}$ (LLZO) electrolytes has high potential to solve the interface problem in next-generation ASSLIBs.[5]

2.2.2 Ceramic Electrolytes (CEs)

Numerous types of Li-ion conducting materials are known so far. Among those are perovskites - $Li_{3x}La_{(2/3)-x}TiO_3$, natrium super ionic conductors (NASICON), lithium super ionic conductors (LISICON) and garnet-type electrolytes. Some important materials and their conductivities as listed by Cao et al. (2014)[9] are given in Table 1.

Table 1. Conductivity of important ceramic electrolytes for ASSLIBs.

Type	Example	Conductivity (S cm^{-1})		Ref.
		RT[(a)]	HT[(b)]	
Perovskite	$Li_{3x}La_{(2/3)-x}TiO_3$ (x = 0.11)	1.0×10^{-3}	5.6×10^{-3} (100 °C)	Stramare et al. (2003)[23]
NASICON	$Li_{1+x}Al_xTi_{2-x}(PO_4)_3$ (x = 0.3)	7.0×10^{-4}	1.1×10^{-2} (100 °C)	Aono et al. (1990)[24]
LISICON	$Li_{14}ZnGe_4O_{16}$	1.0×10^{-7}	1.3×10^{-1} (300 °C)	Hong (1978)[25]
Garnet	$Li_7La_3Zr_2O_{12}$	2.1×10^{-4}	7.1×10^{-4} (75 °C)	Dumon et al. (2013)[26]

[(a)]RT, room temperature; [(b)]HT, high temperature.

Most of the CEs have either high ionic conductivity (for example perovskite lithium–lanthanum–titanates (LLTO)), or high electrochemical stability (i.e. LISICON $Li_{14}ZnGe_4O_{16}$).[10,27] Solid ceramic electrolytes like the garnet-type cubic $Li_7La_3Zr_2O_{12}$ (LLZO) with space group *Ia*-3*d* on the other hand, provide a high Li-ion conductivity (10^{-3} to 10^{-4} S cm^{-1})[10], good thermal and mechanical stability and electrochemical inertness in a wide potential window.[9-11] Rettenwander et al. (2016)[28] reported a high Li-ion conductivity of 1.2×10^{-3} S cm^{-1} for Al and Ga substituted LLZO electrolytes at RT. Because of its superior properties, LLZO (including its variants) is by now one of the most promising solid electrolyte materials and well-suited for the use in SCEs.

2.2.2.a.1 Crystal Stucture of Garnet-type $Li_7La_3Zr_2O_{12}$ (LLZO)

The idealized garnet structure of garnet-type electrolytes is written as $A_3B_2(CO_4)_3$, and consists of AO_8 dodecahedral cages, BO_6 octahedral cages and CO_4 tetrahedral cages.[29] Figure 4 shows the structure of an idealized garnet. Thangadurai et al. (2003)[30] published the first study on Li-stuffed garnets, in which cubic garnet-type $Li_5La_3M_2O_{12}$ (M = Nb, Ta) with an ionic conductivity of 10^{-6} S cm^{-1} was synthesized. Since then, various garnet-type electrolytes have been introduced.

Atomic Sites
$A_3B_2(CO_4)_3$

A – blue
B – orange
C – green

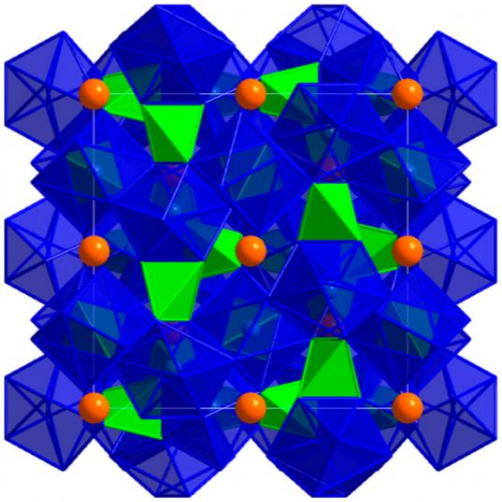

Figure 4. The idealized garnet structure with formula $A_3B_2(CO_4)_3$.[31]

Among those, LLZO is a relatively new discovered garnet that exists in two polymorphs: a cubic phase (*Ia*-3*d*) and a tetragonal phase ($I4_1/acd$) (Figure 5). Murugan et al. (2007)[11] first proposed the high conductive garnet-type cubic phase that hosts 7 Li-ions per chemical formula. At sintering temperatures below 750 °C the less ion-conducting tetragonal phase ($I4_1/acd$ - see Figure 5 (a)) is formed, which is the thermodynamically stable form of pure LLZO at RT.[32] Cubic LLZO exhibits a 100 times higher room-tempereature conductivity ($\sim 10^{-4}$ S cm^{-1}) than tetragonal LLZO ($\sim 10^{-6}$ S cm^{-1}).[10] The high conductivity originates from the uniform movement of Li-ions in x, y, and z directions, whereas the movement of Li-ions is limited to x and y directions in tetragonal LLZO.[33] In the tetragonal phase, there are three available Li-sites, i.e.,

8*a* – tetrahedral
16*f* – octahedral
32*g* – octahedral

In tetragonal LLZO ($I4_1/acd$) the Li-sublattice is ordered. The ordering (all Li sites either full or empty) results in a lower electrostatic energy compared to that in cubic LLZO, because of the reduced coulombic repulsion among Li-ions.[10] Therfore, the tetragonal phase is thermodynamically more stable at RT. In the cubic phase the following sites are available:

24*d* – tetrahedral
48*g* – octahedral
96*h* – octahedral (distorted)

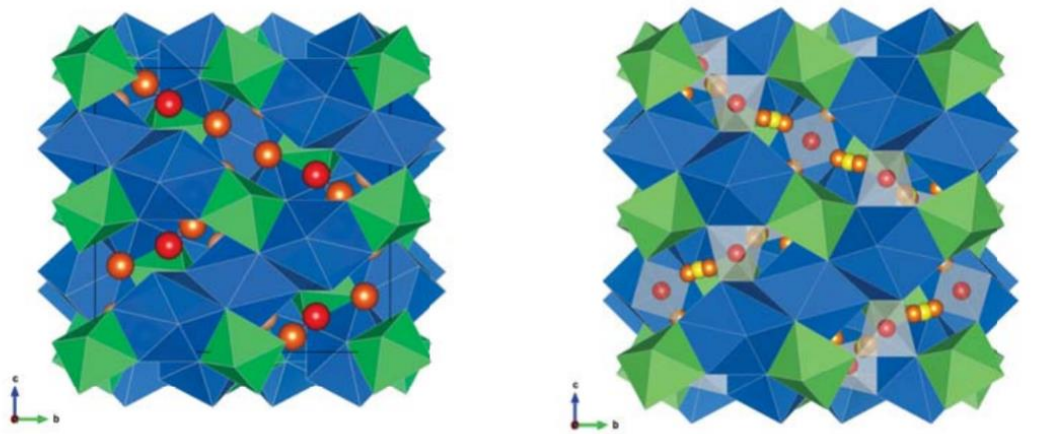

(a) tetragonal phase - $I4_1/acd$ (b) cubic phase – $Ia\text{-}3d$

Figure 5. Crystal structure of tetragonal phase (a) and cubic phase (b) LLZO.[34] Green octahedra indicate BO_6 units (16a) that correspond to ZrO_6 in LLZO. The blue dodecahedra correspond to LaO_8 (24c). (a) In tetragonal LLZO an ordered distribution of Li-ions occupies sites 8*a*, 16*f* and 32*g*. (b) In cubic LLZO the Li-ions are distributed over the tetrahedral and octahedral sites and partially occupy 24*d* (red - spheres), 48*g* (yellow) and 96*h* (orange) sites.

The cubic structure has a shorter bond distance then the tetragonal phase. Consequently, the coulombic repulsion among Li-ions influences the site occupation. When a tetrahedral site (24*d*) is occupied, the adjacent octahedral site (48*g*) can no longer be occupied due to the coulombic effect. The Li-ion has to move on to the next available site (96*h*). Subsequently, the Li-ion diffusion goes along the 24*d* − 96*h* − 24*d* conduction channel.[34] Supervalent doping at the sublattice can stabilize the cubic phase and enhance its Li-ion conductivity. The introduced Li-vacancies increase the entropy and reduce the free energy gain from ordering. Beneath common Al-doping, attention has also been directed to other supervalent cations like Ga^{3+}, Nb^{5+}, Ta^{5+}, etc.[9-11] The effect of substitutional elements stabilizing the cubic structure of LLZO at room temperature is summarized in Table 2.[35]

Table 2. Substitutional elements stabilizing cubic LLZO at room temperature.

Site	**Substitution Element**	**Ref.**
Li	Zn^{2+}, Al^{3+}, Ga^{3+}, Fe^{3+}	[36 – 40]
La	Ce^{4+}	[41]
Zr	Ta^{5+}, Nb^{5+}, Bi^{5+}, Sb^{5+}, Mo^{6+}, Te^{6+}, W^{6+}	[42 – 46]

Amongst the most promising dopant elements, Ga^{3+} stabilizes LLZO at RT with a Li-ion conductivity of 1.3 mS cm^{-1}, which is twice as high as for LLZO stabilized with Al.[34] High energy

densities, however can only be achieved in thin and low weight solid electrolytes.[47] The combination of ceramic ion conductors like Ga-LLZO with solid polymer electrolytes (SPEs) enables a flexible battery design, including the fabrication of thin-film composite electrolytes.

2.2.3 Solid Polymer Electrolytes (SPEs)

The substitution of conventional liquid electrolytes by a plastic material represents a promising class of solid-state ionic conductors. In comparison to CEs, solid polymer electrolytes provide a much better interfacial contact. Especially thin-film polymers are suitable for an all-solid-state system because good contact is easily achieved with soft materials.[48] Polyethylene oxide is a high molecular weight material and its solubility parameters were found to be strongly influenced by certain metal salts.[49] This is important as the lithium salts act as free ions when they dissolve in the matrix. The basic chemical structure of $–[CH_2\text{-}CH_2\text{-}O]–$ in PEO serves as a host matrix for solid electrolytes and the flexible macro-molecular structure of the PEO chains assists the Li-ion transport, as indicated in Figure 6.

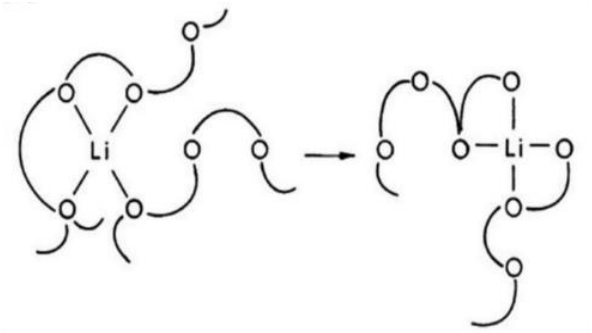

Figure 6. Schematic of Li-ion motion in a polymer-host.[24]

Polymer electrolytes based on PEO require local relaxation and segmental motion of the solvent chains to allow Li-ion transport, and this condition can only be obtained when the polymer is in an amorphous state.[50] Ions can be transferred, following an ion-hopping mechanism as described in Figure 6., with the help of polar groups in polymer chains.[51,52] Thus, the conduction mechanism in SPEs can be seen as a combination of short-range ion hopping and long-range motion of polymer chains.[13]

Generally, Li-salts that have anions with well delocalized charges are preferred because the bulkier the anion of lithium salt, the higher is the ionic conductivity.[53] Among the early introduced lithium salts that have been employed for PEO-based electrolytes are lithium perchlorate ($LiClO_4$), lithium hexafluorosphate ($LIPF_6$), lithium hexafluoroarsenate ($LiAsF_6$) and lithium tetrafluoroborate ($LiBF_4$).[14] The perfluoroalkyl sulfonic-type LiTFSI shows high solubility, high ionic conductivity,

and high electrochemical stability.[14,54] In a system that comprises of PEO and LiTFSI, the salt suppresses crystallization by the introduction of a bulky anion.[12] The typical ionic conductivity of PEO based solid electrolytes is relatively low at room temperature, and reaches practically useful values (of about 10^{-4} S cm^{-1}) only at temperatures of 60–80 °C.[50] By the addition of plasticizers the ionic conductivity of PEO based solid electrolytes can be further increased. One common approach is to add a low molecular weight liquid plasticizers of both cyclic carbonic acid esters and chain-like esters (e.g. propylene carbonate, dimethyl carbonate, diethyl carbonate, etc.) to the PEO matrix.[55] This enables a faster Li-ion transport in PEO by kinetically inhibiting the crystallization and reorganization of the polymer chain at ambient temperature. Nevertheless, most polymer electrolyte-based ASSLIBs can only be used at elevated temperatures due to the low ionic conductivity of polymer electrolytes.[13] To expand the useful operating temperature of the electrolyte, the conduction properties of PEO can be combined with the Li-ion hopping mechanism of CEs in solid conductors.[56]

2.3 Theory of Li-ion Conduction in Solid Composite Electrolytes

The Li-ion transport in solid composite electrolytes can be described by different conduction mechanisms. Arrhenius and Vogel–Tammann–Fulcher (VTF) models are used to quantify the ionic conductivities. For inorganic solid electrolytes, the ionic conductivity can be derived from the motion of vacancies in the crystal lattice or interstitial atoms or ions. Li-ion hopping through connected available vacancies and interstitial sites enables the diffusion of ions in the crystal. In general, the sum of the ionic and electric conductivities gives the specific conductivity of a mixed conducting material:

$$\sigma = n_j q_j \mu_j \tag{2.6.1}$$

where n_j is the number of charge carriers, q_j is the charge and μ_j is the mobility of the conducting species. The sum of the ionic and electric conductivities gives the specific conductivity of a mixed conducting material:

$$\sigma = \sigma_i + \sigma_e \tag{2.6.2}$$

The electronic and ionic contributions of the total conductivity are characterized by the transference numbers:

$$t_i = \frac{\sigma_i}{\sigma} t_e = \frac{\sigma_e}{\sigma} \tag{2.6.3}$$

In inorganic solid electrolytes that use Li-ions as mobile species, the transference number is close to 1. The ionic conduction mechanism with temperature dependence is given by the Arrhenius function:

$$\sigma = Ae^{-E_a/k_B T} \tag{2.6.4}$$

where A is the pre-exponential factor related to the charge carrier, k_B is the Boltzmann constant, and E_a is the activation energy of diffusion.[57] In solid polymer electrolytes, the ion conduction mechanism is more complex due to absence of simple structure-properties relations.[13] An important empirical model used to study the ion transport in polymer electrolytes is the Vogel Tammann–Fulcher (VTF) model. In this model the ionic conductivity can be correlated with the temperature as shown in the following equation:

$$\sigma\,(T) = \sigma_0 T^{-\frac{1}{2}}\, exp\left(-\frac{B}{(T - T_0)}\right) \tag{2.6.5}$$

where B is the activation energy and T_0 is the reference temperature (10-50 K below the glass transition temperature T_g).[58]

2.4 Theoretical Background of the Measurement Techniques

2.4.1 Electrochemical Impedance Spectroscopy (EIS)

The ionic conductivity of solid-state electrolytes can be measured by electrochemical impedance spectroscopy (EIS). In principle low amplitude alternating current (AC) voltages U(t) are applied over a range of frequencies (from Hz to GHz) and the answering current I(t) is measured. The AC current signal response is obtained by the application of sinusoidal potential excitation E(t) (see Figure 7).

The excitation signal can be expressed as a function of time:

$$E(t) = E_0 \sin(\omega t) \tag{2.7.1}$$

with E_0 being the amplitude of the signal and ω the radial frequency ($\omega = 2\pi f$; f = frequency).

In an analogous way the current output can be described by using the radial frequency and the phase shift ϕ.

$$I(t) = I_0 \sin(\omega t + \phi) \tag{2.7.2}$$

The transfer function relating the potential and current signals can be written as an analogous expression to Ohm's law:

$$Z(t) = \frac{E(t)}{I(t)} = \frac{E_0 \sin(\omega t)}{I_0 \sin(\omega t + \phi)} = Z_0 \frac{\sin(\omega t)}{\sin(\omega t + \phi)} \tag{2.7.3}$$

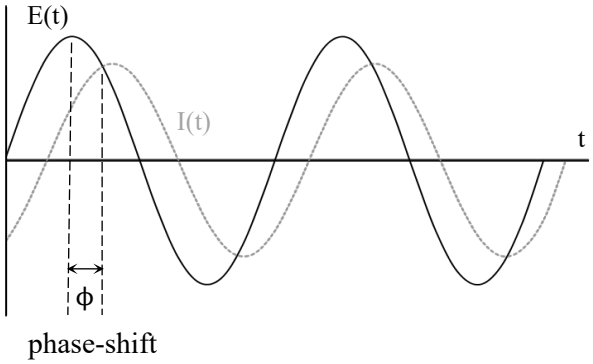

Figure 7. Sinusoidal E(t) and I(t) curves with phase shift **ϕ.**

The impedance is therefore expressed in terms of a magnitude, Z_0, and a phase shift, ϕ.[59] The impedance can also be expressed by the use of complex exponential functions. The complex impedance is given by the following equation:

$$Z(\omega) = Z_0 e^{i\phi} = Z_0(\cos\phi + i \sin\phi) \tag{2.7.4}$$

with $i = \sqrt{-1}$, and $e^{i\phi}$ being the Euler relationship (Equation 2.7.5) of the impedance.

$$e^{i\phi} = \cos\phi + i \cdot \sin\phi \tag{2.7.5}$$

The complex impedance can then be separated into a real (Z') and imaginary part (Z'') of the impedance:

$$Z(\omega) = Z' + i \cdot Z'' \tag{2.7.6}$$

Z' and Z'' can be displayed in a Nyquist plot and are used to determine the the resistances within the material.[60] The Nyquist plot is explained in more detail in chapter **2.4.2.**

2.4.2 Data Presentation of EIS

The Nyquist plot is the most widespread figure for data presentation of EIS. In the Nyquist plot the real impedance is plotted against the imaginary part of the impedance. A typical simple equivalent circuit for a ceramic electrolyte can be divided into three areas (R_{bulk})($R_{gb}Q_{gb}$)($Q_{electrode}$); bulk, grain boundary and electrode. A Nyquist plot of an ideal two point contacted solid electrolyte is shown in Figure 8.

The frequency (ω) dependent relationship between resistance (*R*) and capacitance (*C*) can be represented as given in Equation 2.7.7.[60]

$$\omega RC = 1 \tag{2.7.7}$$

Typical capacitance values for bulk, grain boundary and (ohmic) electrode interface are listed in Table 3.

Table 3. Capacitance (*C*) values and their possible interpration.[61]

Capacitance / F	**Phenomenon Responsible**
10^{-12}	Bulk
10^{-11} – 10^{-8}	Grain boundary
10^{-7} – 10^{-5}	Electrode interface

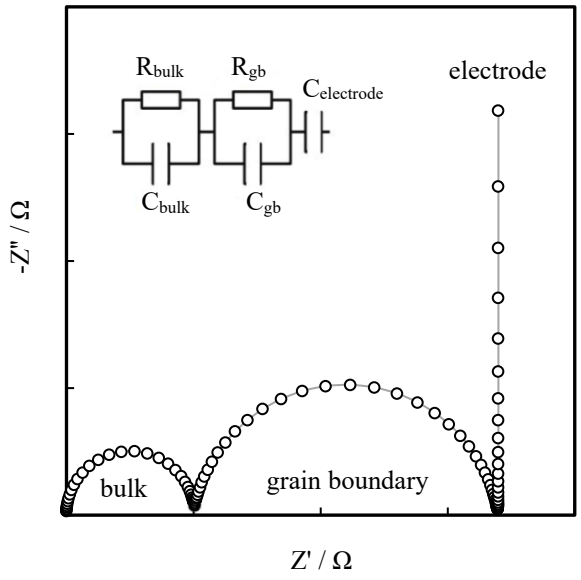

Figure 8. Nyquist plot of an ideal two point contacted solid electrolyte. Three areas can be distinguished: bulk, grain boundary and electrode. *Z'* symbolizes the real impedance in Ω and *-Z''* the complex impedance in Ω. A complete half circle can be displayed as a parallel circuit with electric components.

The capacitance measured in real materials is not ideal, and therefore represented by a constant phase element (CPE) instead of *C*. With the formula from Equation 2.7.8, the bulk and grain-boundary capacitance of a solid electrolyte material can be calculated, where *n* and *Q* are fitted values.

$$C = R^{\left(\frac{1-n}{n}\right)} Q^{\left(\frac{1}{n}\right)} \tag{2.7.8}$$

The ionic conductivity (σ) can be calculated using the formula given in 2.7.6,

$$\sigma = \left(\frac{1}{R}\right)\left(\frac{l}{A}\right) \tag{2.7.9}$$

where σ, *R, l*, and *a* are the conductivity, resistance, thickness and surface area of the analyzed material. Despite the fact that the Nyquist plot is a great tool to describe different types of processes in the material, it does not show frequency information. The frequency dependence of the impedance can be illustrated in a Bode plot. In a Bode plot the impedance is plotted with frequency log ω on the X-axis and both the absolute values of the impedance ($|Z| = Z_0$) and the phase-shift (ϕ) on the Y-axis.[59]

2.5 X-ray Powder Diffraction (XRD)

X-ray powder diffraction (XRD) is a fast, non-destructive technique that is used for phase identification of a crystalline material. The average spacing between layers or rows of atoms is measured, providing information on lattice parameters, average particle size, crystallinity, and crystal defects. The X-rays are generated in a cathode ray tube (Figure 9) by bombarding a target metal with high energy electrons. When the electrons have sufficient energy to dislodge inner shell electrons, outer shell electrons jump to a lower energy shell. These transitions result in specific X-radiation and two types of X-ray spectra are produced.

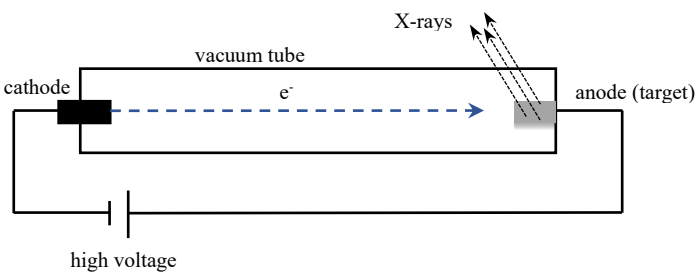

Figure 9. Schematic Depiction of an X-ray Tube.

The characteristic spectra, as a result of specific electronic transitions within the anode material (characteristic X-rays) and the continuous spectra, that consists of a range of wavelengths dependent on the applied voltage across the X-ray tube (Bremsstrahlung).[62]

The filtered monochromatic X-rays (Cu Kα radiation, λ = 1.5418 Å) are directed towards the sample surface, and the crystal planes reflect the X-rays constructively or deconstructively. Constructive interference occurs, when the geometry of the incident X-rays satisfies Bragg's Law (Equation 2.8.1). Bragg's Law gives the condition for a diffracted beam where n, λ, d and θ are the integers representing the order of the diffraction, wavelength of X-rays, inter-planar spacing, and angle of incidence (Bragg angle), respectively.

$$n * \lambda = 2 * d * sin\,\theta \tag{2.8.1}$$

The reflection from successive parallel planes is coherent, if the pathlength difference between the diffracted beams is equal to an integer number of wavelengths. Figure 10 illustrates Bragg's law of powder X-ray diffraction.

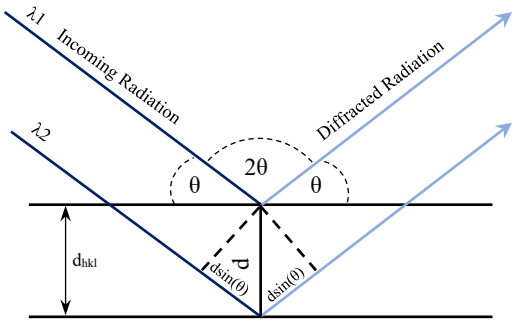

Figure 10. Bragg's Law schematically described. For a crystalline solid, the waves with the wavelength λ of the X-radiation are diffracted from crystal planes with interplanar spacing d, showing the schematics of Bragg's Law (Equation 2.8.1), where d is equal to an integer number of wavelengths for constructive interference. θ is the angle of incidence for the incoming X-ray beam.

The conditions for diffraction can be expressed by the Laue equations (Equation 2.8.2). They relate the incoming waves to the outgoing (diffracted) waves in every direction of the unit cell.

$$a\,(cos\,\Psi_1 - sin\;\varphi_1) = h\,\lambda \qquad b\,(cos\,\Psi_2 - sin\,\varphi_2) = k\,\lambda \qquad c\,(cos\,\Psi_3 - sin\,\varphi_3) = l\,\lambda \tag{2.8.2}$$

a, b, and c correspond to the three crystallographic axes of the crystal and Ψ_i and φ_i are their direction cosines. The angles of the incoming waves are described by $cos\;\Psi_i$; $cos\,\varphi_i$ denotes the

angles of the diffracted waves. λ is the radiation wavelength and h, k and l are the Miller indices of the crystallographic planes. Only if all equations are satisfied, positive interference occurs.
The Miller indices are the reciprocal intercepts of the crystallographic axes.[63] The angle at which reflection can occur for a set of parallel planes is related to the d spacing, according to Bragg's Law. If the wavelength of the X-rays is known, the respective d values can be caluclated. For a cubic unit cell in which the cell parameters obey $a = b = c$, the interplanar spacing d_{hkl} follows:

$$\frac{1}{d_{hkl}^2} = \frac{h^2k^2l^2}{a^2} \tag{2.8.3}$$

Hence, the lattice parameter a can be caluclated from an diffraction pattern in which d and the corresponding Miller indices h, k and l are known.
The observed intensity yields information of the spacing between planes of atoms in the crystal structure. The relative intensity of diffraction peaks is mainly determined by the amount of scattering from $h\ k\ l$ planes in the direction θ, described by the structure factor, F_{hkl}[62]:

$$F_{hkl} = \sum_{n=1}^{N} f_n \exp(2\,\pi\mathrm{i}(hu_n + kv_n + lw_n)) \tag{2.8.4}$$

where the unit cell in the crystal contains N atoms with u, v, and w reduced position indices. f_n is the atomic scattering factor that measures the efficiency of scattering of one atom. The atomic scattering factor is dependend on the scattering angle θ.

3 MATERIALS AND MATERIALS CHARACTERIZATION

In the following points **3.1-3.2** all devices and chemicals that were used for the preparation and characterization of the synthesized substances are listed.

3.1 Chemicals

- Lithium carbonate (≥ 99% purity), Sigma-Aldrich
- Lanthanum oxide (99.95%,), Hoechst AG
- Gallium(III)oxide (99.995 % purity), Alfa Aesar
- Zirconium(IV)oxide (99%), Sigma-Aldrich
- 3-glycidyloxypropyl)trimethoxysilane (≥98 %), Sigma-Aldrich
- Polyethylene oxide (Mw = 400 000 g mol^{-1}), Sigma-Aldrich
- Lithium bis(trifluoromethanesulfonyl)imide (99.95% purity), Sigma-Aldrich
- 1,8-Diazabicyclo(5.4.0)undec-7-ene (98 %), Sigma-Aldrich
- Divinyl sulfone (≥ 96 %), Sigma-Aldrich
- 2-Buten-1,4-diol (97 %), Sigma-Aldrich
- Acetonitrile (99.8 %), Sigma-Aldrich
- Ethanol (≥ 99.8 %), Sigma-Aldrich
- Isopropyl alcohol (≥ 98 %), Sigma-Aldrich
- Hot-pressed $Li_{6.75}La_3Zr_{1.75}Ta_{0.25}O_{12}$ (Ø 1 cm, 2 mm thickness), Toshima Manufacturing

3.2 Equipment

- Ball mill, FRITSCH Pulverisette 7
- Oven, Nabertherm
- MSK-110 Hydraulic Press, MTI Corporation
- Femto Plasma Cleaner, Diener Electronic
- High vacuum sputter coater, Leica EM QSG100
- X-ray diffractometer, Bruker D8-Advance
- Broadband dielectric analyser, Novocontrol Concept 80
- NMR spectrometer, Bruker Advance III
- Double-furnace DSC, PerkinElmer DSC 8500

3.3 Characterization of Powders and Solid Electrolytes

3.3.1 X-ray Powder Diffraction (XRD)

In this work, X-ray diffraction was mainly used for the primary characterization to confirm the structure of the synthesized materials. Phase analysis was performed by X-ray powder diffraction experiments under air with a Bruker D8-Advance X-ray powder diffractometer and a Lynxeye detector. A copper target was used (Cu Kα radiation, Bragg−Brentano (θ−θ) geometry) and angles of 2θ from 10 to 80° were measured.

3.3.2 Nuclear Magnetic Resonance (NMR) Spectroscopy

NMR measurements were carried out with a Bruker Advance III 300 MHz spectrometer (1H: 300.36 MHz; 13C: 75.53 MHz) at 25 °C. The probes were dissolved in deuterated chloroform ($CDCl_3$), purchased from Cambridge Isotope Laboratories, Inc.

3.3.3 Differential Scanning Calorimetry (DSC)

The melting points of the electrolytes were determined via DSC analysis (PerkinElmer DSC 8500) under nitrogen atmosphere from -50 °C to 200 °C with a heating rate of 20 °C min^{-1}.

3.3.4 Electrochemical Impedance Spectroscopy (EIS)

The ionic conductivity was measured by EIS. The measurements were carried out by a Concept 80 system (Novocontrol) with a Novocontrol Alpha analyser. Single-sweep measurements at room temperature were done in the frequency range from 10 mHz to 10 MHz. For the measurement, the Ga-LLZO powder was pressed into pellets (Figure 11). A press with a diameter of 10 mm was used and a load of 0.3 tons was applied for 3 minutes. The thickness of the pellets varied from 5 – 8 mm. Chemical vapour deposition with Au was carried out at 10^{-5} mbar until a layer thickness of 100 nm was reached (Leica EM QSG100 sputter coater).

4 EXPERIMENTAL

4.1 Synthesis of Ga-doped LLZO Ceramic Electrolyte

Gallium-doped $Li_7La_3Zr_2O_{12}$ solid electrolytes were synthesized via a conventional solid-state method based on the procedure described by Wagner et al.[34]. Stoichiometric amounts of Li_2CO_3 (≥ 99 %), La_2O_3 (99.95 %, preheated at 900 °C for 12 h), ZrO_2 (99 %) and Ga_2O_3 (≥ 99 %) were ground and mixed in an agate mortar under addition of isopropyl alcohol. To reach the intended stoichiometry 10 wt.% excess Li_2CO_3 (≥ 99 %) was added to compensate the loss of lithium during annealing. After drying, the mixture was pressed into pellets and heated to 850 °C with a rate of 5 °C min^{-1} and calcinated for 4 h. In the next step the pellets were again grounded in an agate mortar and ball-milled for 1 h under isopropyl alcohol using zirconia balls (180 ZrO_2 balls, Ø 5 mm) at 500 rpm. After drying, the powder was pressed into pellets (Ø 1 cm, 5 mm thickness) using a hydraulic press.

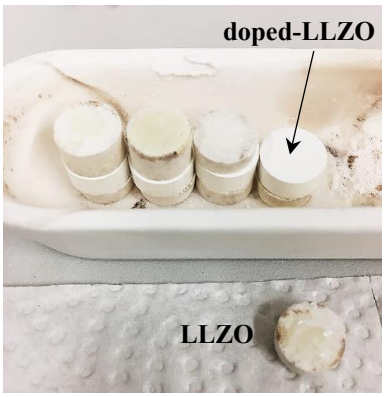

Figure 11. Ga-LLZO pellets between two pure pellets of LLZO.

In order to lower the loss of lithium during annealing and to avoid the incorporation of Al^{3+} from the crucible, an embedding sintering method was used. The sample pellets were placed between two additional pellets of pure LLZO (Figure 11), which supplied the doped-LLZO with lithium and lowered the effect of the lithium loss phenomena during the sintering process. The obtained Ga-LLZO pellets were further processed by ball-milling (4 h, 500 rpm, 180 ZrO_2 balls, Ø 5 mm) with isopropyl alcohol as a solvent medium. The final resulting slurry was dried thoroughly at 60 °C for 24 hours. In a final step the pellets were heated with a rate of 5 °C min^{-1} to 1230 °C and sintered for 6 h in ambient air. The crystalline structure was evaluated by XRD and the ionic conductivity was measured by EIS.

4.2 Surface Modification with 3-Glycidyloxypropyl)trimethoxysilane (Si-R)

4.2.1 Surface Modification of Ga-LLZO Ceramic Particles

Activation of the surface terminated oxygen of Ga-LLZO particles was achieved by a dry etching process (O_2, 60 seconds). To avoid any degradation under ambient atmosphere, the activated ceramic nanoparticles were immediately immersed in a solution of 10 mL Si-R and 40 mL Ethanol. After 16 h of continuous stirring (300 rpm, Ar atmosphere), the coated Ga-LLZO was filtered from the solution, and dried in a drying chamber at 60 °C for 24 h.

4.2.2 Surface Modification of the LLZTO pellet and Preparation of Bilayer Cells

A commercially hot-pressed LLZTO pellet (Ø 1 cm, 2 mm thickness) was used for the preparation of Bilayer Cells. Before each experiment, the pellet was polished with SiC grinding paper (no. 1000 – no. 4000) to ensure that any degradation layers are removed. Afterwards, a 100-nm-thick gold electrode was applied on one side of the pellet with a Leica EM QSG100 high vacuum sputter. The other side of the pellet was either

(1) plasma treated for 60 s,
(2) plasma treated for 60 s and immediately immersed in a solution of Si-R as described in Section **4.2.1** for 16 hours,
(3) or kept pristine.

In the next step the bilayer cells were casted with a polymer electrolyte and cured over night. The polymer electrolyte was prepared by dissolving 90 wt.% PEO (M_w = 400 000 g mol^{-1}) and 10 wt. % LiTFSI in anhydrous acetonitrile by stirring (300 rpm) at 90 °C for 12 h. The thickness of the polymer electrolyte was about 300 µm. All experiments were performed in an Ar-filled glovebox. The synthesis route is illustrated in Figure 12.

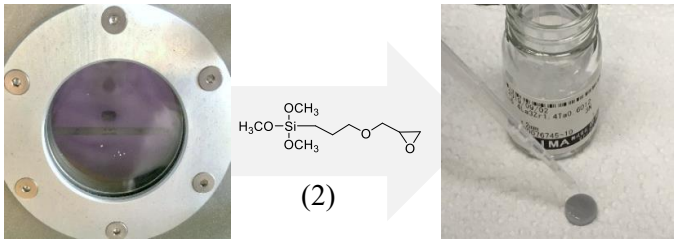

Figure 12. Synthesis route for bilayer cells. In (1) the LLZTO pellets are plasma-treated for 60 s. (2) represents the solution casting of the pellets with Si-R and in (3) the polymer electrolyte is casted on the bilayer cells.

4.3 Synthesis of a Sulfone-based Polymer Electrolyte (OMP)

For the production of the Oxa-Michael Product (OMP) a 1,8-Diazabicyclo(5.4.0)undec-7-ene (DBU) mediated polyaddition of divinyl sulfone (DVS) and 2-Buten-1,4-diol was carried out under solvent-free conditions as described by Strasser et al. (2017)[64]. DBU (25.5 mg, 0.01675 mmol, 0.4105 equiv.) was dissolved in 2-Buten-1,4-diol (362.8 mg, 4.11 mmol) and subsequently DVS (482.0 mg, 4.08 mmol) and LiTFSI (1; 5; 7.5; 10; 12.5 wt.%) were admixed under stirring at room temperature. The reaction scheme is shown in Figure 13.

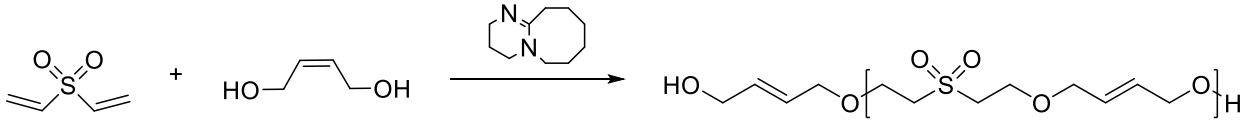

Figure 13. Reaction between 2-buten1,4-diol and DVS with DBU as catalysator.

As soon as the DVS was added for 1-2 min, an exothermic reaction was observed. The light brown reaction mixture (Figure 14) was placed in a drying chamber at 60 °C for 24 h and an aliquot was removed and investigated by ^{1}H-NMR spectroscopy (see Figure 20).

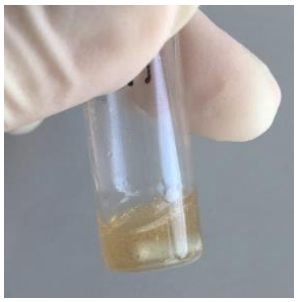

Figure 14. Picture of the OMP with 10 wt.% LiTFSI content after 24 h in the drying chamber.

4.4 Synthesis of Mixed Polymer Electrolyte- and Solid Composite Membranes

The following procedures were carried out in an argon-filled glovebox. The membranes were prepared by a solution-casting method. For the mixed PEs, the amount of OMP added varied between one and 40 wt.%. For the composites, different fractions of Ga-LLZO were added (from one to 50 wt.%). The ratio of [EO]/[Li] was fixed at 18:1. Calculated amounts of either:

(1) PEO(LiTFSI) and OMP (1; 10; 20; 30; 35; 40 wt.%),
(2) PEO(LiTFSI) and Ga-LLZO (or modified Ga-LLZO) or
(3) PEO(LiTFSI) and Ga-LLZO (or modified Ga-LLZO) and OMP (35 wt.%)

were dissolved and dispersed in anhydrous acetonitrile by constant stirring (300 rpm) at 90 °C for 12 h. The polymer suspension was cast on a flat teflon plate and the solvent was allowed to evaporate slowly. The film was dried in vacuum at 40 °C for 12 h and homogeneous and mechanically stable membranes with thickness in the range of 130 to 150 µm were obtained. The synthesis route for (2) is shown in Figure 15.

(1) (2) (3)

Figure 15. Synthesis route for solid composites: (1) A polymer suspension of PEO:Ga-LLZO 70:30 wt.% is casted on a teflon plate (2) and composite membranes (Ø 8 mm; thickness 150) are cut out with a stamping tool (3).

5 RESULTS AND DISCUSSION

In this chapter, all measured data are summarized and the findings are analyzed and compared with literature. First, the structural and electrochemical properties of LLZO are discussed. Moreover, the compositional dependence of the Li-ion transport in PEO:Ga-LLZO composites is investigated and the optimum filler concentration is analyzed. Afterwards, the visualisation of modified LLZO particles in composites is investigated in LLZTO|Si-R|PEO bilaminar cells. In a last step, OMP is introduced as a plasticizer and its role in advanced solid composites is outlined.

5.1 Ceramic Electrolytes

Powder XRD was used to identify the phase of synthesized Ga-LLZO particles and EIS measurements were carried out to analyze the electrochemical properties of Gallium- and Tantalum-doped LLZO pellets.

5.1.1 Primary Characterization with X-ray Powder Diffraction

After the sintering process, a powder XRD pattern was recorded to evaluate the phase composition and identify the crystal structure within the synthesis. Figure 16 shows the powder XRD pattern, obtained from the Ga-LLZO sample sintered at 1230 °C for 6 h (blue line, top).

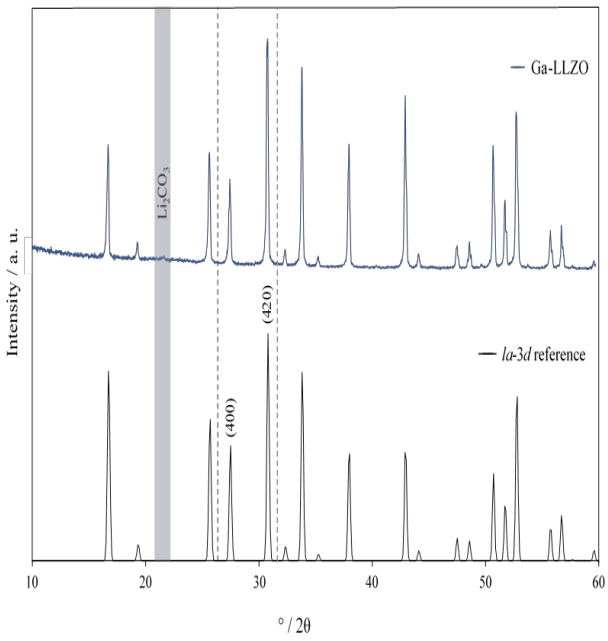

Figure 16. Powder XRD pattern of Ga-doped $Li_7La_3Zr_2O_{12}$ (blue line, top) and reference cubic (*Ia*-3*d* space group) pattern (ICSD #422259) shown at the bottom. The Ga-LLZO sample sintered at 1230 °C shows cubic (*Ia*-3*d* space group) symmetry with diffraction peaks indicating cubic (400) and (420) planes.

As referenced in the inorganic crystal structure database (ICSD #422259), the Ga-LLZO can be indexed as cubic with *Ia*-3*d* space group. The two diffraction peaks in $27° < 2\theta < 32°$, as marked by the dashed lines in Figure 16, indicate cubic (400) and (420) planes respectively. As shown by Han et al. (2020)[65], sintering at a lower temperature leads to the formation of the tetragonal (*I*41/*acd*) polymorph, resulting in a splitting of the diffraction peaks due to symmetry reduction. The reflex at approximately $2\theta = 21°$ indicates a minor amount of Li_2CO_3, which is most likely due to surface reactions with moisture and carbon dioxide since the measurement was performed in air. This result suggests, that gallium incorporation and sintering at 1230 °C stabilizes the cubic phase of LLZO at room temperature, as reported in literature.[34] The cubic lattice parameter of Ga-LLZO is 12.9612 Å, which agrees well with that of cubic LLZO synthesized at a similar temperature in literature.[34]

5.1.2 Conductivity Measurements

Conductivity measurements of LLZTO and Ga-LLZO were made using electrochemical impedance spectroscopy (EIS) over the frequency range of 10 mHz to 10 MHz (see Section **3.3.4**). The impedance spectra of LLZTO (Figure 17 (a)) shows a high-frequency semicircle, attributed to the bulk (see below), followed by a low-frequency response from the electrode. In the impedance spectra of Ga-LLZO (Figure 17 (b)), besides the high- and low frequency contribution an additional arc due to grain boundaries may be hidden in the small shoulder of the electrode response.

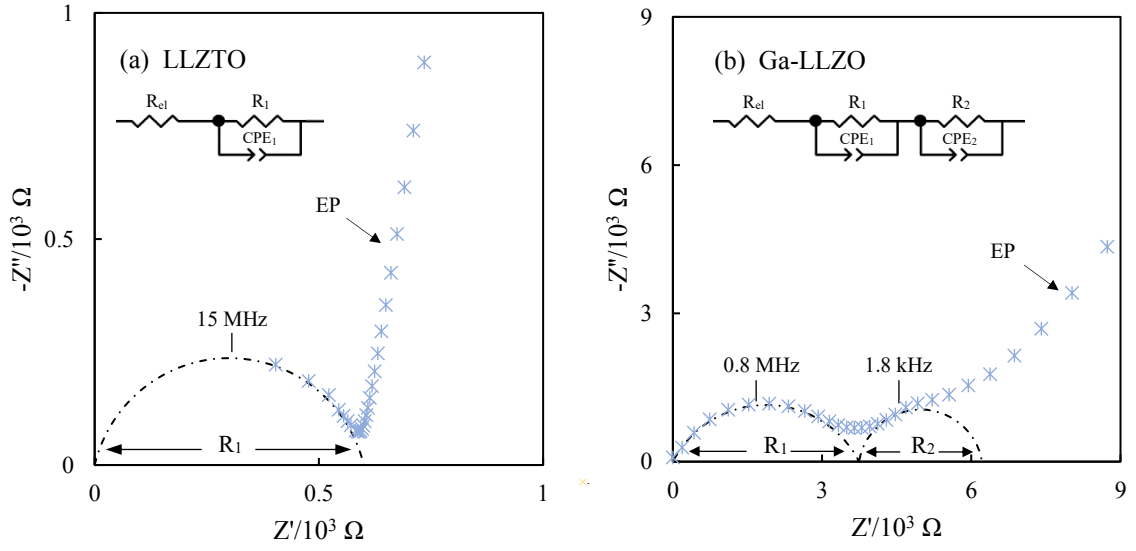

Figure 17. Nyquist plot of (a) LLZTO and (b) Ga-LLZO measured at 20 °C. The dashed lines represent the fitted semicircles, observed by EIS. Electrode polarization (EP) takes place in the low-frequency spike of the nyquist plots.

To quantify the spectra they were fitted based on an equivalent circuit model. First, the bulk resistance could be obtained via fitting the high frequency semicircle to a single $R_1||CPE_1$ element. For the second semicircle in the mid-frequency range of the Ga-LLZO spectra, an additional $R_2||CPE_2$ element has to be added. The corresponding Li-ion conductivity (σ) can be calculated according to Eq. 2.7.9. Table 4 summarizes the calculated values of the conductivity and the capacitance from the fitted Nyquist plots in Figure 17.

Table 4. Calculated values of conductivity and capacitance based on the impedance spectra from Figure 17.

	LLZTO	**Ga-LLZO**
R_1 [Ω]	576	3745
σ_1 [mS cm^{-1}]	0.44	0.43
n_1[a]	0.9	0.8
C_1 [F cm^{-2}]	2×10^{-11}	1.6×10^{-12}
R_2 [Ω]	-	2470
σ_2 [mS cm^{-}]	-	0.65
n_2	-	0.9
C_2 [F cm^{-2}]	-	8×10^{-9}
σ_{total} [mS cm^{-1}]	0.44	0.26

[a]non-ideality factor of the capacitance

For LLZTO the high-frequency component fitted to a single $R_1||CPE_1$ element is 2×10^{-11} F cm^{-2}. The capacitance value of 2×10^{-11} F cm^{-2} can be assigned to a grain boundary process.[66] The calculated total Li-ion conductivity of 0.44 mS cm^{-1} is similar to values reported in literature.[43] In case of the Ga-LLZO, the high-frequency arc gives a capacitance of 1.6×10^{-12} F cm^{-2}. According to literature, a realistic value for the bulk capacitance of an oxide is typically in the pF range.[61] Hence, the capacitance value for the high frequency component in Ga-LLZO can be assigned to a bulk process. The second mid-frequency component fitted to an additional $R_2||CPE_2$ element has a capacitance of 8×10^{-9} F cm^{-2}. The capacitance of the mid-frequency contribution sits within the range expected for a grain boundary process. The calculated total Li-ion conductivity of Ga-LLZO yields a value of 0.26 mS cm^{-1}, which is in agreement with values reported in literature.[31]

The Ga-LLZO particles were used as inorganic fillers in composite materials in order to enhance the mechanical strength and Li-ion conductivity. The effect of filler content on the electrochemical properties in PEO:Ga-LLZO composites is discussed in the following section.

5.2 Optimization of the Ga-LLZO Content in PEO:Ga-LLZO Composites

The influence of different amounts of the Ga-LLZO particles in PEO:Ga-LLZO composites on the Li-ion transport behaviour is presented in Figure 18, and the respective Li-ion conductivities are listed in Table 5.

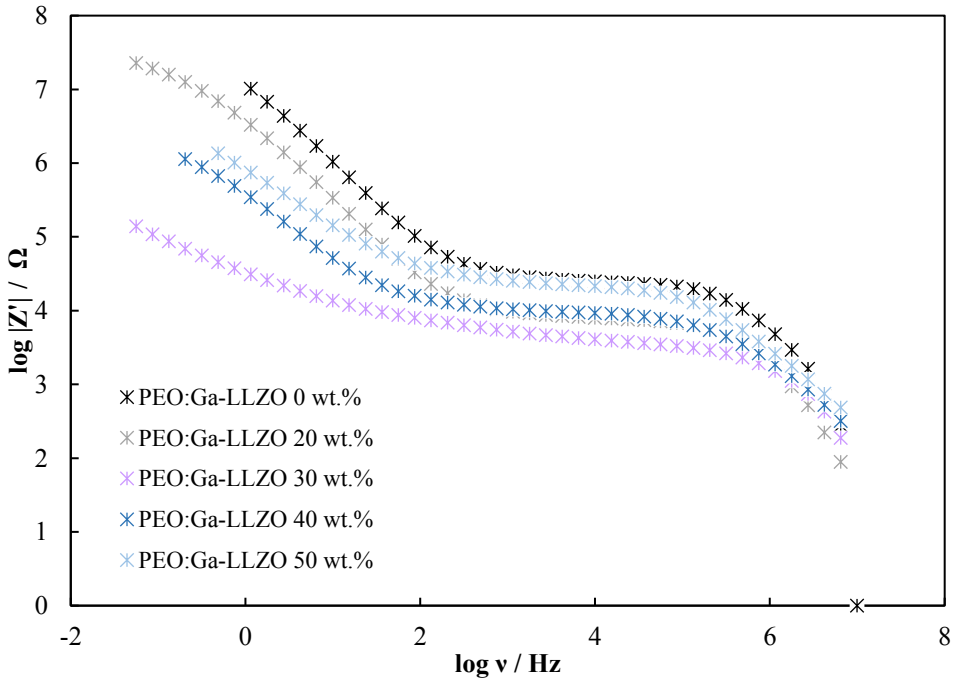

Figure 18. Bode plot of the electrochemical impedance for PEO:Ga-LLZO composites with different composition, measured at 20 °C.

Table 5. Bulk Resistance and room-temperature Li-ion conductivity of PEO:Ga-LLZO composites with different composition.

	R / Ω	**σ_{total} / S cm^{-1}**
PEO	2.5×10^{4}	9.5×10^{-7}
PEO:Ga-LLZO 20 wt.%	8.5×10^{3}	3.5×10^{-6}
PEO:Ga-LLZO 30 wt.%	3.3×10^{3}	9.0×10^{-6}
PEO:Ga-LLZO 40 wt.%	9.5×10^{3}	3.1×10^{-6}
PEO:Ga-LLZO 50 wt.%	2.2×10^{4}	1.3×10^{-6}

The observed trend in the ionic conductivity regarding the Ga-LLZO content in the SCEs can be explained by taking in account the compositional dependence of the three determining factors: ion

mobility, ion transport pathways, and active ion concentration.[15] In this work, the highest ionic conductivity was found in SCEs with 30 wt.% Ga-LLZO filler, the further increase of filler amount resulted in a lower ionic conductivity. The addition of filler enhances the ionic conductivity of the SCEs due to rapid Li-ion conduction via the inorganic conductor itself or the interfaces formed between polymer and filler.[13] Agglomerated clusters of nanoparticles significantly decrease the volume ratio of the interface. Consequently, most of the bulk polymer phase cannot be converted to highly-conductive interfacial phase, leading to a decreased ionic conductivity at high filler-concentrations.[13] The observed behaviour is typical for solid composites.[15,16] The maximum filler ratio varies in a large range and is dependent on the composition of the composites. Li et al. (2019)[16] reported a maximal conductivity of 7.2×10^{-5} S cm^{-1} at 30 °C for PEO:16 vol% Ga-LLZO composite electrolytes. The results visible in Figure 18 show, that with an increase in the fraction of ceramic Ga-LLZO phase in the PEO:Ga-LLZO composites up to 30 wt.%, the ionic conductivity increases. A higher content of Ga-LLZO in the polymer matrix leads to a decrease in ionic conductivity. In this work, a Li-ion conductivity of 9.0×10^{-6} S cm^{-1} at 20 °C was achieved for PEO:Ga-LLZO 30 wt. %.

Preliminary work showed, that the surface modification of oxide surfaces can improve the compatibility and adhesion between the ceramic particles and the polymeric matrix.[67] For this reason, bilaminar cells of surface-modified LLZTO and PEO were made to investigate if the modification of LLZO ceramic surfaces can negate the interfacial resistance, and further enhance the Li-ion transport properties in PEO:LLZO composites. The results are shown in Section **5.3**.

5.3 Bilayer Cells

Bilayer cells of LLZTO|PEO, LLZTO|P|PEO and LLZTO|P|Si-R|PEO were prepared and impedance spectroscopy was used to study the Li-ion transport across the interphase. Each of the semicircles presented in Figure 19 can be fitted by a constant phase element (CPE), in parallel to a resistance element Because no electrode polarization is observed in the spectrum of LLZTO|PEO, a single R|CPE is used to fit the semicircle. The low-frequency spike in the spectra of LLZTO|P|PEO and LLZTO|P|Si-R|PEO can be fitted by two serial-connected R|CPE element.

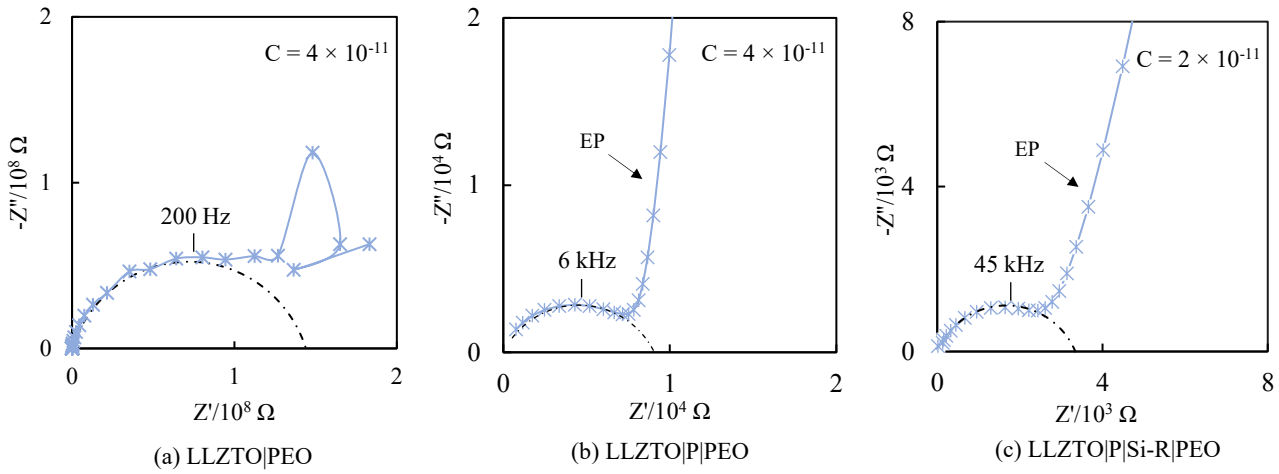

Figure 19. Nyquist Plots of LLZTO|PEO (a), LLZTO|plasma etching (P)|PEO (b) and LLZTO|plasma etching (P)|Si-R|PEO (c) measured at 20 °C. The dashed lines represent the fitted semicircles, observed by EIS. No electrode polarization (EP) is observed in spectrum (a).

The electrical contribution of both components is approximately constant, as all geometric and compositional parameters were kept fixed during assembling of the cells. Therefore, any change in the resistance of the bilaminar cell (R_{lam}) is related to the interfacial resistance (R_{int}). R_{int} is given by $R_{lam} = R_{LLZTO} + R_{PEO} + R_{int}$, and the corresponding ASR is given by $ASR = R_{int} A$. The calcuclated values for grain, grain boundary and interfacial resistance are listed in Table 6. The creation of an interface between LLZTO and PEO leads to a significant increase in R_{lam} from about 30 kΩ to 83 MΩ caused by the high charge transfer resistance between LLZTO and PEO (R_{int}) of ASR = 42 MΩcm^2. For LLZTO|P|PEO, the resistance R_{lam} decreases by more than three orders of magnitude. The obtained ASR value of 32 kΩ cm^2 could be explained by an increased bonding between PEO segments to the LLZTO particles. This bonding lowers the free volume between the PEO particles and LLZTO, and enhances the Li-ion transport across the interface.

Table 6. Grain, Grain Boundary, and Interfacial Resistance.[5]

	ρ / Ω cm	**C / pF cm $^{-2}$**	**n**	**σ_{total} / S cm^{-1}**
Single components				
LLZTO	576*	0.2	0.9	0.44
PEO	2.9×10^4*	0.2	0.8	0.002
Surface Modification				
LLZTO|PEO	8.4×10^7	0.4	0.9	
LLZTO|P|PEO	8.3×10^4	0.4	0.8	
LLZTO|P|SI-R|PEO	3.0×10^4	0.2	0.8	

*Resistance values (Ω)

A further reduction of the ASR by an order of magnitude to a value of about 500 Ω cm^2 at 20 °C can be seen for the functionalized LLZTO|P|Si-R|PEO bilayer cell. The bifunctional Si-R-molecule acts as linking agent between the polymeric matrix and the surface of the LLZTO, by forming covalently bonded Si-R layers. The Si-R units screen the surface polarity (oxygen density) that reduces the electrostatic repulsion between LLZTO and PEO. Consequently a significantly improved charge transfer can be achieved across the LLZTO|PEO interface.[5]

Gupta et al. (2019)[68] suggest, that an ASR smaller than 100 Ω cm^2 is required to enable Li-ion transport over the whole volume fraction of a composite electrolyte. Various approaches exist to enhance the ionic charge transport across the interface.[69] In this work the LLZTO|PEO interface has been reduced to 500 Ω cm^2 at 20 °C by plasma activation and covalent surface modification of the LLZTO surface. The modification of ceramic surfaces with Si-R offers great potential to improve composite electrolytes towards the integration in future solid-state Li batteries.

5.4 Effect of OMP as Plasticizer in Solid Composites

To further enhance the Li-ion conductivity, OMP was used as a plasticizer in advanced composite electrolytes. Therefore, plasticized PEO:OMP mixed polymer electrolytes were analyzed and the LiTFSI- and OMP-content in the polymer system were optimized.

5.4.1 Primary Characterization of the Oxa-Michael Product (OMP)

The DBU-mediated polymerization between DVS and 2-Buten-1,4-diol was observed with ^{1}H NMR spectroscopy (300 MHz, $CDCl_3$, 25 °C). Figure 20 shows the ^{1}H NMR spectrum of OMP.

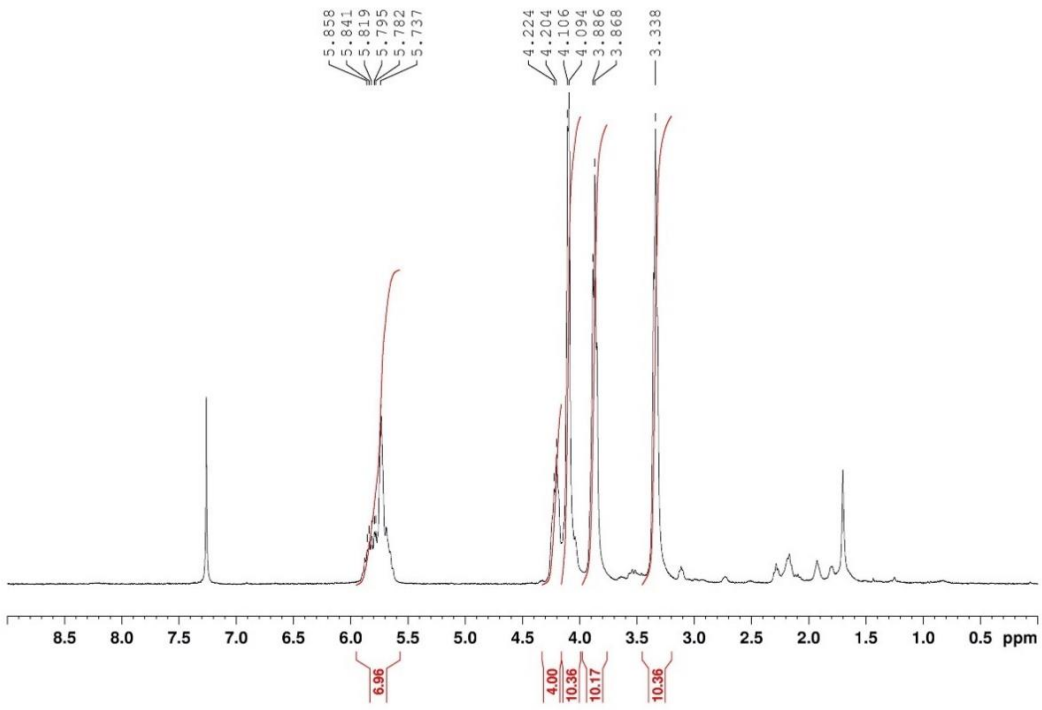

Figure 20. ^{1}H NMR spectrum of the sulfone-based polymer electrolyte (OMP)

The signal at 7.3 ppm is related to $CDCl_3$ whereas the peak at 1.7 ppm results from residual DBU, which was used as a catalyst. The signal at 4.2 ppm refers to the alcoholic end groups of the polymer (OH-CH_2-CH=$CHCH_2$) and the signal at 5.74 is related to (CH_2CH_2=$CHCH_2$) in the chain. The peaks at 3.34 and 3.87 confirm the sulfonyl group in the polymeric backbone (SO_2-CH_2-CH_2-O). The chain length (n) can be calculated from the ratio between the number of repeating units vs. the integral per proton value of the alcoholic end chain. The relatively low value of n = 2.54 is due to a slight excess of 2-Buten-1,4-diol in the reaction. The calculated M_w value for the OMP is ≤ 500 g mol^{-1}. Other experiments were carried out with a 1:1 molar ratio of DVS to 2-Buten-1,4-diol, which lead to a longer polymer chain n = 6.15, a M_w value ≤ 800 g mol^{-1} and

sulfonic end groups (OMP_2 see Appendix Figure 25).[64] The OMP with the lower chain length shows low viscosity and stickiness at room temperature. The OMP_2 with the higher chain length is more brittle.

The general rule in designing high Li-ion conducting SPEs is to suppress the crystallinity in order to maximize the mobile phase. Therefore, a low glass transition temperature (T_g) is crucial to enable the segmental motion of polymer chains.[54-52] If the T_g is low enough, more amorphous regions are available at ambient temperature. The glass transition temperature determined from the DSC measurement is -42.2 °C. (see Appendix Figure 26). Stolwijk et al. (2013)[70] reported experimental T_g values for PEO:LiTFSI complexes in the range from -45 to -60 °C. Diverse T_g behavior as a function of salt-concentration has been reported in literature.[70] Since the Li-ion conductivity depends on the Li-salt-concentration, an ideal polymer host must have the ability to dissolve lithium salts at ambient temperature and allow the fast motion of free ions in the media.

5.4.2 Salt-concentration Dependence of the Li-ion Conductivity in OMP

The salt-concentration dependence of the ionic conductivity of OMP with salt-concentration of 1.0 – 12.5 wt.% has been investigated via EIS and the results are shown in Figure 21. If the salt content is increased, the number of free ions increases, thereby increasing conductivity.[71] However, several studies observed a decrese in Li-ion conductivity, as the salt-concentration exceeds its saturation level.[14,70]

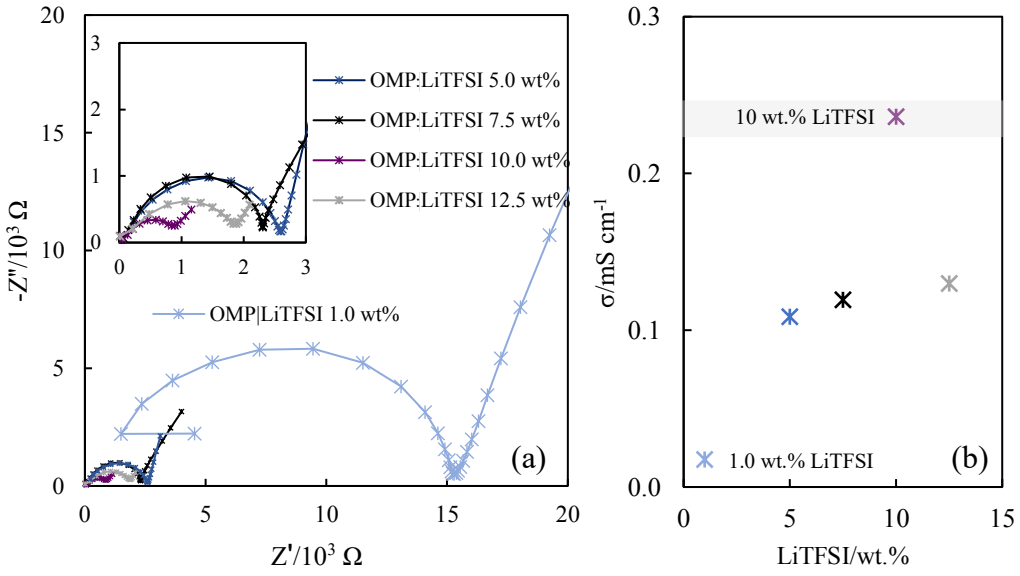

Figure 21. (a) Nyquist plot of OMP with different concentrations of LiTFSI measured at 20 °C; (b) variation of Li-ion conductivity as a function of salt-concentration in wt.%.

The calculated conductivity values, corresponding to the respective molar ratios (PEO:LiTFSI) for the data shown in Figure 21 are listed in Table 7. The OMP containing one wt.% shows an ionic conductivity of 1.75×10^{-5} S cm^{-1}. A significant increase of one order of magnitude can be observed up to 10 wt.% LiTFSI in the OMP. The linear increase with salt addition up to a value of 10 wt.% results from the increased number of charge carriers in the dilute region. Higher amounts of salt in the polymer matrix result in a decrease of ionic conductivity due to ion pairing and physical crosslinking between polymer chain and Li-ions. The ion pairing effect with increasing LiTFSi content has been optically observed by the accompanied stiffening of electrolyte material. A LiTFSI content ≤ 12.5 wt.% results in an inhomogeneous mixture of OMP and Li-salt due to a disfavoured salt dilution and can not be further fabricated.

Table 7 Salt-concentration dependence of the Li-ion conductivity at 20 °C.

wt. % LiTFSI	**LiTFSI:OMP**	**σ / S cm^{-1}**
1	2:100	1.8×10^{-5}
5	1:10	1.1×10^{-4}
7.5	1.5:10	1.2×10^{-4}
10	2:10	2.4×10^{-4}
12.5	2.5:10	1.3×10^{-4}

Maurel et al. (2020)[72] reported the highest conductivity (3.79×10^{-6} S cm^{-1} at 20 °C) for SPEs containing LiTFSi and PEO ($M_w \sim 100.000$ g mol^{-1}) in a ratio of 1:10. OMP shows its maximum conductivity (2.4×10^{-4} S cm^{-1} at 20 °C) at a salt content twice as high (LiTFSI:OMP 2:10). The lowering of the Li-ion conductivity with regard to the molecular weight of the polymers can be explained by the relatively large number of chain end units in short-chain polymer matrices.[73,74] The low M_w of the OMP leads to more free volume and higher segmental flexibility. However, it was not possible to fabricate the OMP into free-standing membranes, due to its sticky behavior. Therefore, polymer blends of high molecular weight PEO and low molecular weight OMP were made as described in the following section.

5.4.3 Mixed Polymer Electrolytes (PEO(LiTFSI):OMP)

SPEs of pure PEO show a two orders of magnitude lower Li-ion conductivity than OMP. Therefore, OMP was used as a plastizicer in PEO:OMP polymer blends to alter the Li-ion conducting properties. By the substitution of high-molecular-weight PEO with low-molecular-weight OMP the mechanical properties of the mixed polymer blends changed significantly, becoming much more soft, flexible and stickier. The compositional dependence of the Li-ion conductivity was investigated by EIS and the calculated conductivity values were plotted against the ratio of PEO:OMP in Figure 22 (b).

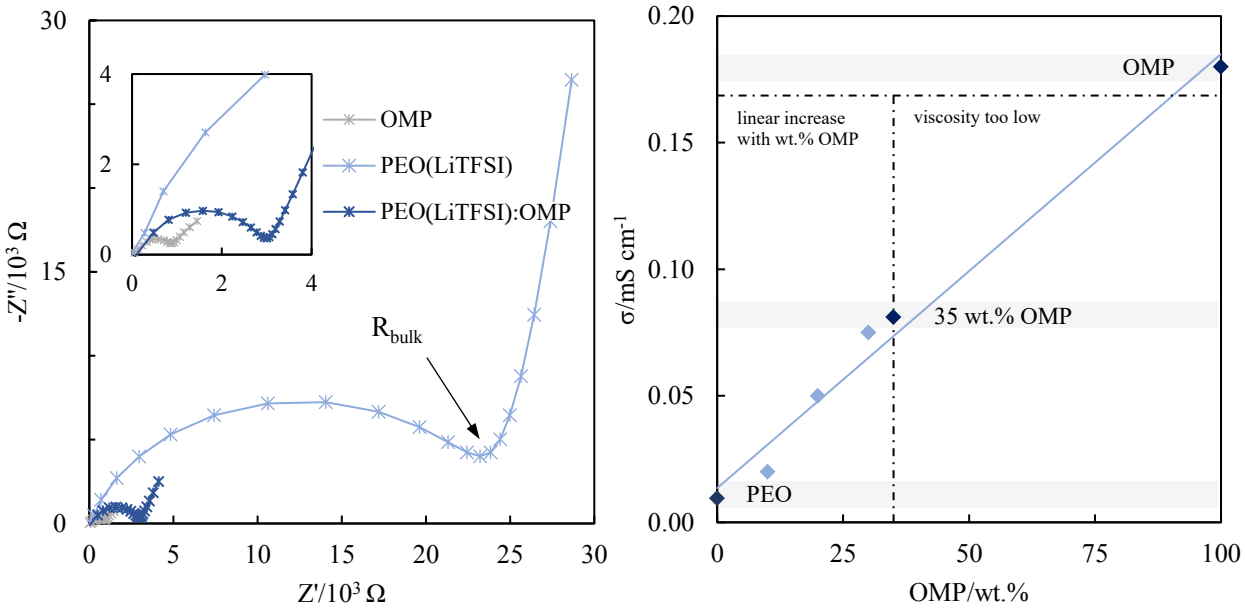

(a) Nyquist plot of mixed SPEs

(b) OMP-dependent Conductivity

Figure 22. Electrochemical Impedance spectra (a) for PEO(LiTFSI), PEO(LiTFSI):OMP and OMP at 20 °C and (b) Li-ion conductivity dependence on the wt.% of plasticizer (OMP) in mixed SPEs. .

The Nyquist plots for PEO(LiTFSI), PEO(LiTFSI):OMP (containing 35 wt.% of the OMP) and OMP are shown in Figure 22 (a). The Nyquist plots of the mixed polymer electrolytes were fitted by an equivalent circuit model consisting of a single $R_1||CPE_1$ element. The conductivity of mixed SPEs increases linearly up to an amount of 35 wt.% OMP added. Further addition leads to high stickiness and low viscosity of the SPEs, and therefore complicates further processing steps. The respective Li-ion conductivity values for PEO(LiTFSI), PEO(LiTFSI):OMP and OMP are shown in Table 8.

Table 8. Bulk resistance and Li-ion conductivity of PEO(LiTFSI), PEO(LiTFSI):OMP and OMP

	wt.% OMP	**R / Ω**	**σ / S cm^{-1}**
PEO(LiTFSI)	0	2.5×10^{4}	2.0×10^{-6}
PEO(LITFSI):OMP	35	3.2×10^{3}	5.1×10^{-6}
OMP	100	957	1.8×10^{-5}

The partial substitution of PEO by 35 wt.% OMP results in a 10-fold better conductivity compared with pure PEO SPEs. As the ionic conductivity strongly depends on the morphology of the electrolyte, the increase in conductivity with OMP addition can be explained in terms of enhancement of the amorphous phase. The decrease in the PEO-crystallinity can be interpreted on the basis of chain flexibility, which is reflected by a lowered T_g.[75] This is suggestive of enhanced segmental motions at higher contents of OMP. A reduction in the energy barrier to the segmental motion of Li-ions is achieved. Despite the high Li-ion conductivity at ambient conditions, the PEO:OMP SPEs show poor mechanical properties.

For PEO(LiTFSI):OMP mixed PEs, the ionic conductivity was found to linearly increase with plasicizer concentration. In order to test if this is also true for PEO:Ga-LLZO composites, OMP was used as plasticizer in advanced SCEs.

5.5 Advanced Solid Composite Electrolytes

The findings of the previous Sections **5.1–5.4** were used to synthesize advanced composites, consisting of modified Ga-LLZO particles and plasticized PEO:OMP polymer electrolytes. In composites with low interfacial resistance, the Li-ion transport takes place in both phases, resulting in a faster conduction process than in composites with high interfacial resistance (where the Li-ion transport only takes place in the polymer phase). Therefore, one would expect, that composites containing surface-modified Ga-LLZO particles exhibit a higher Li-ion conductivity compared to composites with untreated ceramic. The electrochemical behaviour of composites containing modified- and unmodified Ga-LLZO particles respectively was studied with EIS are displayed in the Nyquist plots of Figure 23.

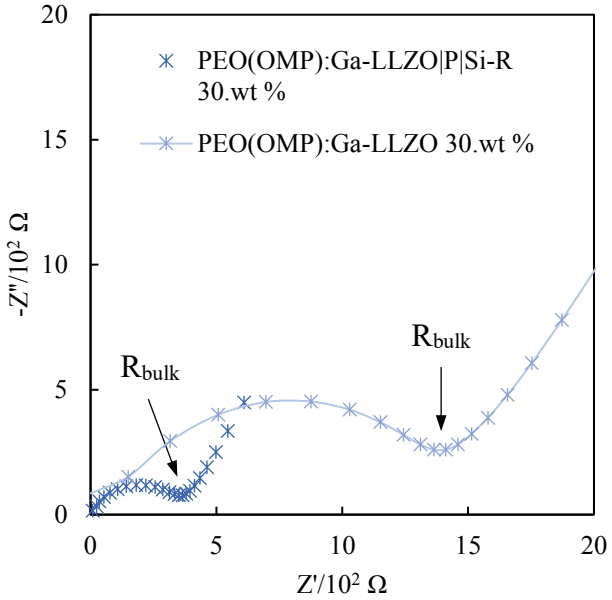

Figure 23. Nyquist Plots of advanced PEO(OMP):Ga-LLZO 30 wt.% and PEO(OMP):Ga-LLZO|P|Si-R 30.wt.% composites measured at 20 °C.

Table 9. Bulk Resistance and room-temperature Li-ion conductivity of advanced solid composites

	R / Ω	**σ_{total} / S cm^{-1}**
PEO(OMP):Ga-LLZO 30 wt.%	1.4×10^3	2.1×10^{-5}
PEO(OMP):Ga-LLZO|P|Si-R 30.wt %	3.6×10^2	8.3×10^{-5}

The spectra of PEO(OMP):Ga-LLZO 30 wt.% and PEO(OMP):Ga-LLZO|P|Si-R 30.wt % in Figure 23 are composed of a single semicircle followed by a low-frequency spike that can be fitted by two serial-connected R||CPE elements. PEO(OMP):Ga-LLZO|P|Si-R 30 wt. %, containing surface modified Ga-LLZO particles, shows a higher room-temperature conductivity (8.3×10^{-5} S

cm^{-1}) compared with that of PEO(OMP):Ga-LLZO 30 wt.% (2.1×10^{-5} S cm^{-1}). The observed behaviour confirms the hypothesis discussed in Section **5.3**. The increased bonding between polymer segments and surface-activated Ga-LLZO particles enables a fast Li-ion conduction across the lowered interface. As expected, the addition of OMP in PEO(OMP):Ga-LLZO 30 wt.%, alters ion transport pathways and increases the ion mobility, thus further enhancing the ionic conductivity. PEO(OMP):Ga-LLZO 30 wt.% composites exhibit a Li-ion conductivity of 2.1 x 10^{-5} S cm^{-1}, whereas unplasticized composites of the same composition show a lower conductivity (9.0×10^{-6} S cm^{-1}, see Section **5.2**). The high Li-ion conduction in OMP in combination with the beneficial Li-ion transport across the interface enables the preparation of advanced SCEs with great electrochemical and mechanical properties.

5.5.1 Arrhenius Plot of Advanced Solid Composite Electrolytes

Because lower activation energy directly correlates to faster Li-ion diffusion, a low activation energy for ionic diffusion throughout the electrolyte material is of primary importance.[76] The temperature-dependent behaviour of the advanced SCEs was investigated via EIS and the results are displayed in an Arrhenius diagram (Figure 24).

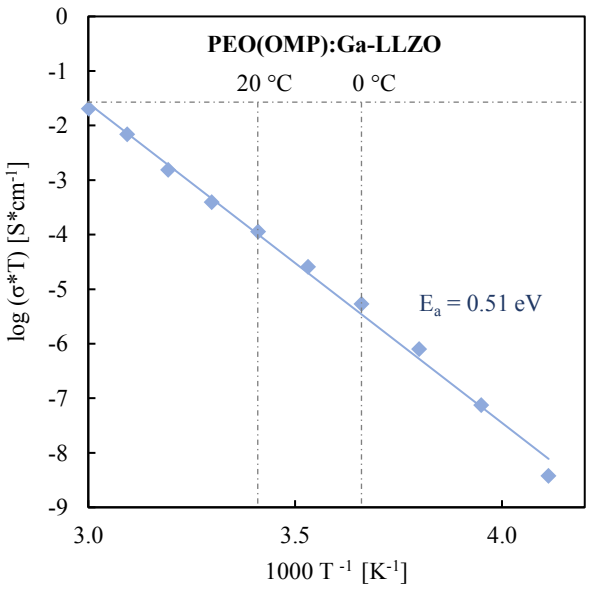

Figure 24. Arrhenius plot of PEO(OMP):Ga-LLZO composite electrolytes in the temperature range of -30 °C to 60 °C.

PEO(OMP):Ga-LLZO (containing 30 wt.% Ga-LLZO as active filler) composites show linear Arrhenius behavior in the temperature range of -30 °C to 60 °C. The activation energy (E_a) of the composites is calculated according to $\sigma = Ae^{-E_a/k_BT}$. The activation energy of the advanced

PEO(OMP):Ga-LLZO composites is 0.51 eV. In general, the activation energy value found in this work is lower than values reported in literature on PEO:Ga-LLZO and PEO:LLZTO composites (0.59-0.62 eV).[16,77] This indicates easier ionic conduction pathways in ternary composite materials containing a plasticizer, compared to composites without one. Similar behaviour was reported by Al-Salih et al. (2020)[78], where the activation energy dropped by about 0.1 eV to a value of ~ 0.41 eV when Succinonitrile (SN) was used as a solid plasticizer in composites comprising of PEO, SN and LLTO as an active filler.

6 CONCLUSION

The high interfacial resistance across the ceramic|polymer interface in solid composite electrolytes (SCEs) hinders the development of high-performance all-solid-state Li-ion batteries (ASSLIBs). Therefore, a facile surface modification technique was introduced in this work to address this problem. The glass transition temperature, ionic conductivity, ceramic|polymer interfacial behavior and Arrhenius behaviour were investigated using Differnetial Scanning Calorimetry (DSC) and Electrochemical Impedance Spectroscopy (EIS). The compositional dependence of the Li-ion conductivity was investigated by variation of the Ga-LLZO content in the polymer matrix.

The results showed, that with an increase in the fraction of ceramic Ga-LLZO phase in the PEO:Ga-LLZO composites up to 30 wt.%, the ionic conductivity increased. A higher content of Ga-LLZO in the polymer matrix lead to a decrease in ionic conductivity. EIS analysis of LLZTO|PEO and surface modified LLZTO|P|Si-R|PEO bilayer cells revealed the contribution of LLZTO grain boundaries to the electrolyte resistance. The ceramic|polymer interfacial resistance decreased from 83 MΩ to 30 kΩ when surface modification techniques were applied. The lowered interfacial resitance enables the preferential path for Li-ion conduction across the interface and through the ceramic phase. A fast conduction porocess is provided due to a reduction of the free volume between the PEO particles and LLZTO. The further incorporation of a high-ion conducting sulfone-polymer electrolyte (OMP) in the SCEs contributed to the improved Li-ion conducting properties, by lowering the T_g and enhancing the suppression of crystallinity in the polymer phase.

The modification of ceramic Ga-LLZO particles with Si-R leads to a lowered ASR in PEO:LLZO composites that enables a fast charge transfer across the interface. In combination with the high-Li-ion conducting properties of low-viscous OMP, SCEs with a Li-ion conductivity of 8.3×10^{-5} S cm^{-1} at 20 °C were synthesized, which makes them promising electrolytes for the next generation of ASSLIBs. Future work in this area will focus on extensive battery testing at high current densities and further optimzation of the properties of the electrolytes. More detailed investigation of the OMP_2 with the higher chain length (Appendix Figure 25) will also be required, because surface modification might be achieved by the sulfone-functionalized end groups of the polymer if used in solid composite electrolytes.

7 APPENDIX

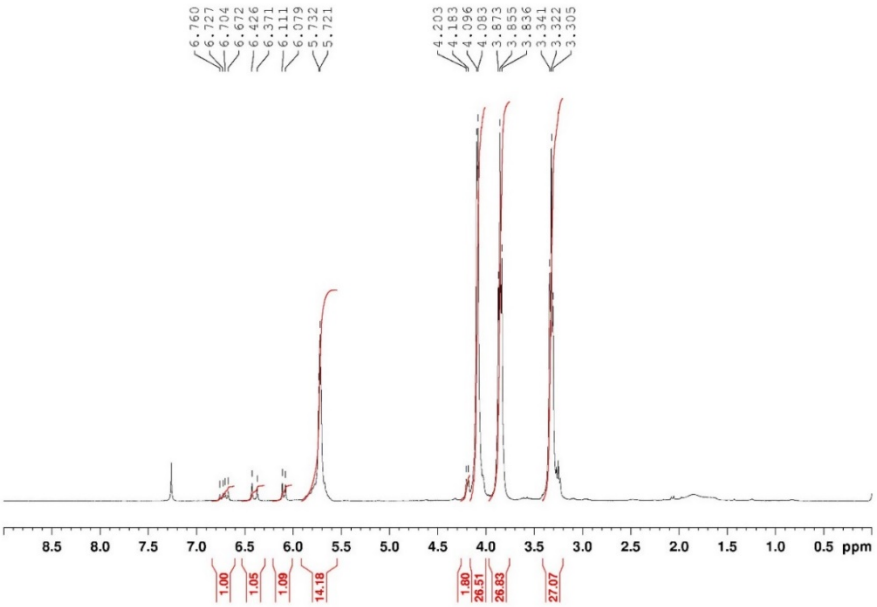

Figure 25. ^{1}H NMR spectrum of the sulfon-polymer electrolyte with higher chain length (OMP_2). Data provided by Susi Fischer (ICTM, TU Graz)

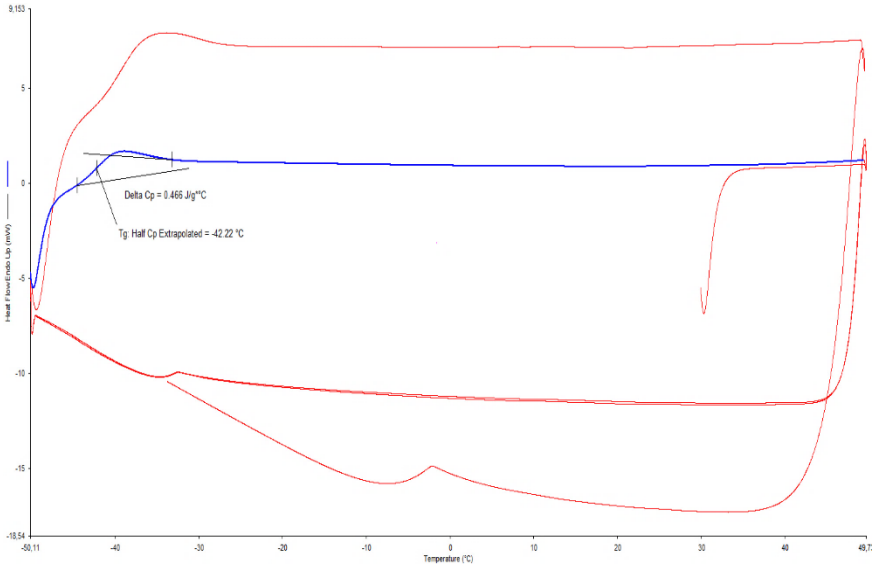

Figure 26. DSC of the sulfon-based polymer electrolyte (OMP_1), used as plasticizer in advanced solid composite electrolytes (SCEs).

BIBLIOGRAPHY

1. Janek J, Zeier WG. A solid future for battery development. *Nat Energy*. 2016;1(9):16141. doi:10.1038/nenergy.2016.141

2. Safari M. Battery electric vehicles: Looking behind to move forward. *Energy Policy*. 2018;115:54-65. doi:10.1016/j.enpol.2017.12.053

3. Li S, Jiang M, Xie Y, Xu H, Jia J, Li J. Developing High-Performance Lithium Metal Anode in Liquid Electrolytes: Challenges and Progress. *Adv Mater*. 2018;30(17):1706375. doi:10.1002/adma.201706375

4. Li S, Zhang S, Shen L, et al. Progress and Perspective of Ceramic/Polymer Composite Solid Electrolytes for Lithium Batteries. *Adv Sci*. 2020;7(5):1903088. doi:10.1002/advs.201903088

5. Kuhnert E, Ladenstein L, Jodlbauer A, et al. Lowering the Interfacial Resistance in Li6.4La3Zr1.4Ta0.6O12|Poly(Ethylene Oxide) Composite Electrolytes. *Cell Rep Phys Sci*. Published online September 2020:100214. doi:10.1016/j.xcrp.2020.100214

6. Roth EP, Orendorff CJ. How Electrolytes Influence Battery Safety. *Interface Mag*. 2012;21(2):45-49. doi:10.1149/2.F04122if

7. Sun Y-K. Promising All-Solid-State Batteries for Future Electric Vehicles. *ACS Energy Lett*. 2020;5(10):3221-3223. doi:10.1021/acsenergylett.0c01977

8. Tatsumisago M, Nagao M, Hayashi A. Recent development of sulfide solid electrolytes and interfacial modification for all-solid-state rechargeable lithium batteries. *J Asian Ceram Soc*. 2013;1(1):17-25. doi:10.1016/j.jascer.2013.03.005

9. Cao C, Li Z-B, Wang X-L, Zhao X-B, Han W-Q. Recent Advances in Inorganic Solid Electrolytes for Lithium Batteries. *Front Energy Res*. 2014;2. doi:10.3389/fenrg.2014.00025

10. Kim A, Woo S, Kang M, Park H, Kang B. Research Progresses of Garnet-Type Solid Electrolytes for Developing All-Solid-State Li Batteries. *Front Chem*. 2020;8:468. doi:10.3389/fchem.2020.00468

11. Murugan R, Thangadurai V, Weppner W. Fast Lithium Ion Conduction in Garnet-Type Li7La3Zr2O12. *Angew Chem Int Ed*. 2007;46(41):7778-7781. doi:10.1002/anie.200701144

12. Marzantowicz M, Dygas JR, Krok F, et al. Crystallization and melting of PEO:LiTFSI polymer electrolytes investigated simultaneously by impedance spectroscopy and polarizing microscopy. *Electrochimica Acta*. 2005;50(19):3969-3977. doi:10.1016/j.electacta.2005.02.053

13. Dirican M, Yan C, Zhu P, Zhang X. Composite solid electrolytes for all-solid-state lithium batteries. *Mater Sci Eng R Rep*. 2019;136:27-46. doi:10.1016/j.mser.2018.10.004

14. Manuel Stephan A. Review on gel polymer electrolytes for lithium batteries. *Eur Polym J*. 2006;42(1):21-42. doi:10.1016/j.eurpolymj.2005.09.017

15. Zheng J, Hu Y-Y. New Insights into the Compositional Dependence of Li-Ion Transport in Polymer–Ceramic Composite Electrolytes. *ACS Appl Mater Interfaces*. 2018;10(4):4113-4120. doi:10.1021/acsami.7b17301

16. Li Z, Huang H-M, Zhu J-K, et al. Ionic Conduction in Composite Polymer Electrolytes: Case of PEO:Ga-LLZO Composites. *ACS Appl Mater Interfaces*. 2019;11(1):784-791. doi:10.1021/acsami.8b17279

17. Pujari SP, Scheres L, Marcelis ATM, Zuilhof H. Covalent Surface Modification of Oxide Surfaces. *Angew Chem Int Ed*. 2014;53(25):6322-6356. doi:10.1002/anie.201306709

18. Onclin S, Ravoo BJ, Reinhoudt DN. Engineering Silicon Oxide Surfaces Using Self-Assembled Monolayers. *Angew Chem Int Ed*. 2005;44(39):6282-6304. doi:10.1002/anie.200500633

19. Sagiv' J. Organized Monolayers by Adsorption, I . Formation and Structure of Oleophobic Mixed Monolayers on Solid Surfaces. :7.

20. Hoepfner JC, Pezzin SH. Functionalization of carbon nanotubes with (3-glycidyloxypropyl)-trimethoxysilane: Effect of wrapping on epoxy matrix nanocomposites. *J Appl Polym Sci*. 2016;133(47). doi:10.1002/app.44245

21. Håkansson A, Han S, Wang S, et al. Effect of (3-glycidyloxypropyl)trimethoxysilane (GOPS) on the electrical properties of PEDOT:PSS films. *J Polym Sci Part B Polym Phys*. 2017;55(10):814-820. doi:10.1002/polb.24331

22. Ebnesajjad S. *Surface Treatment of Materials for Adhesive Bonding*.; 2014.

23. Stramare S, Thangadurai V, Weppner W. Lithium Lanthanum Titanates: A Review. *Chem Mater*. 2003;15(21):3974-3990. doi:10.1021/cm0300516

24. Aono H, Sugimoto E, Sadaoka Y, Imanaka N, Adachi G. Ionic Conductivity of Solid Electrolytes Based on Lithium Titanium Phosphate. *J Electrochem Soc*. 1990;137(4):1023-1027. doi:10.1149/1.2086597

25. Hong HY-P, Laboratory L. CRYSTAL STRUCTURE AND IONIC CONDUCTMTY OF Lil4Zn(GeO4) 4 A N D O T H E R N E W Li+ S U P E R I O N I C C O N D U C T O R S. 13(2):8.

26. Dumon A, Huang M, Shen Y, Nan C-W. High Li ion conductivity in strontium doped Li7La3Zr2O12 garnet. *Solid State Ion*. 2013;243:36-41. doi:10.1016/j.ssi.2013.04.016

27. Reddy MV, Julien CM, Mauger A, Zaghib K. Sulfide and Oxide Inorganic Solid Electrolytes for All-Solid-State Li Batteries: A Review. *Nanomaterials*. 2020;10(8):1606. doi:10.3390/nano10081606

28. Rettenwander D, Redhammer G, Preishuber-Pflügl F, et al. Structural and Electrochemical Consequences of Al and Ga Cosubstitution in Li $_7$ La $_3$ Zr $_2$ O $_{12}$ Solid Electrolytes. *Chem Mater*. 2016;28(7):2384-2392. doi:10.1021/acs.chemmater.6b00579

29. Thangadurai V, Narayanan S, Pinzaru D. Garnet-type solid-state fast Li ion conductors for Li batteries: critical review. *Chem Soc Rev*. Published online 2014:14.

30. Thangadurai V, Kaack H, Weppner WJF. Novel Fast Lithium Ion Conduction in Garnet-Type Li5La3M2O12 (M = Nb, Ta). *J Am Ceram Soc*. 86(3):4.

31. Thangadurai V, Pinzaru D, Narayanan S, Baral AK. Fast Solid-State Li Ion Conducting Garnet-Type Structure Metal Oxides for Energy Storage. *J Phys Chem Lett*. 2015;6(2):292-299. doi:10.1021/jz501828v

32. J. D. Percival. *Synthesis and Characterisation of Novel Lithium Ion Containing Garnet-Related Materials for Potential Lithium Ion Battery Applications*. PhD Thesis. University of Surrey; 2009.

33. Chen F, Li J, Huang Z, Yang Y, Shen Q, Zhang L. Origin of the Phase Transition in Lithium Garnets. *J Phys Chem C*. 2018;122(4):1963-1972. doi:10.1021/acs.jpcc.7b10911

34. Wagner R, Redhammer GJ, Rettenwander D, et al. Crystal Structure of Garnet-Related Li-Ion Conductor Li $_{7-3x}$ Ga $_{x}$ La $_{3}$ Zr $_{2}$ O $_{12}$: Fast Li-Ion Conduction Caused by a Different Cubic Modification? *Chem Mater*. 2016;28(6):1861-1871. doi:10.1021/acs.chemmater.6b00038

35. A. Wachter-Welzl. *The Composition-Dependent Conductivity of Li7La3Zr2O12 Ceramics Investigated by Spatially Resolved Impedance Spectroscopy*. PhD Thesis.; 2017.

36. Geiger CA, Alekseev E, Lazic B, et al. Crystal Chemistry and Stability of "Li $_{7}$ La $_{3}$ Zr $_{2}$ O $_{12}$ " Garnet: A Fast Lithium-Ion Conductor. *Inorg Chem*. 2011;50(3):1089-1097. doi:10.1021/ic101914e

37. Rawlence M, Filippin AN, Wac A, Rupp JLM, Buecheler S. Effect of Gallium Substitution on Lithium-Ion Conductivity and Phase Evolution in Sputtered Li7−3xGaxLa3Zr2O12 Thin Films. *ACS Appl Mater Interfaces*. Published online 2018:9.

38. Rettenwander D, Welzl A, Cheng L, Suard E. Synthesis, Crystal Chemistry, and Electrochemical Properties of Li7−2xLa3Zr2−xMoxO12 (x = 0.1−0.4): Stabilization of the Cubic Garnet Polymorph via Substitution of Zr4+ by Mo6+. *Inorg Chem*. Published online 2015:10.

39. Rettenwander D, Geiger CA, Tribus M, Tropper P, Amthauer G. A Synthesis and Crystal Chemical Study of the Fast Ion Conductor Li7−3xGaxLa3 Zr2O12 with x = 0.08 to 0.84. *Inorg Chem*. Published online 2014:6.

40. Rettenwander D, Geiger CA, Amthauer G. Synthesis and Crystal Chemistry of the Fast Li-Ion Conductor Li $_{7}$ La $_{3}$ Zr $_{2}$ O $_{12}$ Doped with Fe. *Inorg Chem*. 2013;52(14):8005-8009. doi:10.1021/ic400589u

41. Rangasamy E, Wolfenstine J, Allen J, Sakamoto J. The effect of 24c-site (A) cation substitution on the tetragonal–cubic phase transition in Li7−xLa3−xAxZr2O12 garnet-based ceramic electrolyte. *J Power Sources*. 2013;230:261-266. doi:10.1016/j.jpowsour.2012.12.076

42. Ohta S, Kobayashi T, Seki J, Asaoka T. Electrochemical performance of an all-solid-state lithium ion battery with garnet-type oxide electrolyte. *J Power Sources*. 2012;202:332-335. doi:10.1016/j.jpowsour.2011.10.064

43. Allen JL, Wolfenstine J, Rangasamy E, Sakamoto J. Effect of substitution (Ta, Al, Ga) on the conductivity of Li7La3Zr2O12. *J Power Sources*. 2012;206:315-319. doi:10.1016/j.jpowsour.2012.01.131

44. Dhivya L, Janani N, Palanivel B, Murugan R. Li $^{+}$ transport properties of W substituted Li $_{7}$ La $_{3}$ Zr $_{2}$ O $_{12}$ cubic lithium garnets. *AIP Adv*. 2013;3(8):082115. doi:10.1063/1.4818971

45. Ramakumar S, Satyanarayana L, Manorama SV, Murugan R. Structure and Li+ dynamics of Sb-doped Li7La3Zr2O12 fast lithium ion conductors. *Phys Chem Chem Phys*. 2013;15(27):11327. doi:10.1039/c3cp50991e

46. Deviannapoorani C, Dhivya L, Ramakumar S, Murugan R. Lithium ion transport properties of high conductive tellurium substituted Li7La3Zr2O12 cubic lithium garnets. *J Power Sources*. 2013;240:18-25. doi:10.1016/j.jpowsour.2013.03.166

47. Judez X, Eshetu GG, Li C, Rodriguez-Martinez LM, Zhang H, Armand M. Opportunities for Rechargeable Solid-State Batteries Based on Li-Intercalation Cathodes. *Joule*. 2018;2(11):2208-2224. doi:10.1016/j.joule.2018.09.008

48. Armand M. The history of polymer electrolytes. *Solid State Ion*. 1994;69(3-4):309-319. doi:10.1016/0167-2738(94)90419-7

49. Lundberg RD, Bailey FE, Callard RW. Interactions of inorganic salts with poly(ethylene oxide). *J Polym Sci [A1]*. 1966;4(6):1563-1577. doi:10.1002/pol.1966.150040620

50. Croce F, Appetecchi GB, Persi L, Scrosati B. Nanocomposite polymer electrolytes for lithium batteries. 1998;394:3.

51. Cohen MH, Turnbull D. Molecular Transport in Liquids and Glasses. *J Chem Phys*. 1959;31(5):1164-1169. doi:10.1063/1.1730566

52. Gibbs JH, DiMarzio EA. Nature of the Glass Transition and the Glassy State. *J Chem Phys*. 1958;28(3):373-383. doi:10.1063/1.1744141

53. Xue Z, He D, Xie X. Poly(ethylene oxide)-based electrolytes for lithium-ion batteries. *J Mater Chem A*. 2015;3(38):19218-19253. doi:10.1039/C5TA03471J

54. Yi J, Guo S, He P, Zhou H. Status and prospects of polymer electrolytes for solid-state Li–O $_{2}$ (air) batteries. *Energy Environ Sci*. 2017;10(4):860-884. doi:10.1039/C6EE03499C

55. Manuel Stephan A, Nahm KS. Review on composite polymer electrolytes for lithium batteries. *Polymer*. 2006;47(16):5952-5964. doi:10.1016/j.polymer.2006.05.069

56. Fergus JW. Ceramic and polymeric solid electrolytes for lithium-ion batteries. *J Power Sources*. Published online 2010:17.

57. Fan L, Wei S, Li S, Li Q, Lu Y. Recent Progress of the Solid-State Electrolytes for High-Energy Metal-Based Batteries. *Adv Energy Mater*. 2018;8(11):1702657. doi:10.1002/aenm.201702657

58. Sun C, Liu J, Gong Y, Wilkinson DP, Zhang J. Recent advances in all-solid-state rechargeable lithium batteries. *Nano Energy*. 2017;33:363-386. doi:10.1016/j.nanoen.2017.01.028

59. Copyright 1990-2016 © Gamry Instruments, Inc. *Application Note Rev.*; 2016.

60. Barsoukov E, Macdonald JR, eds. Impedance Spectroscopy Theory, Experiment, and Applications. In: *Impedance Spectroscopy*. 1st ed. Wiley; 2005. doi:10.1002/0471716243.fmatter

61. Irvine JTS, Sinclair DC, West AR. Electroceramics: Characterization by Impedance Spectroscopy. *Adv Mater*. 1990;2(3):132-138. doi:10.1002/adma.19900020304

62. Krischner, H., Koppelhuber-Bitschnau, B. *Röntgenstrukturanalyse Und Rietveldmethode*. Vieweg; 1994.

63. Oppermann H. Grundlagen der Festkörperchemie. Von A. R. West. VCH Verlagsgesellschaft, Weinheim, 1992. XII, 455 S., Broschur DM 58.00 — ISBN 3-527-28103-7. *Angew Chem*. 1992;104(9). doi:10.1002/ange.19921040950

64. Strasser S, Wappl C, Slugovc C. Solvent-free macrocyclisation by nucleophile-mediated oxa-Michael addition polymerisation of divinyl sulfone and alcohols. *Polym Chem*. 2017;8(11):1797-1804. doi:10.1039/C7PY00152E

65. Han J, Kim JC. A solid-state route to stabilize cubic Li7La3Zr2O12 at low temperature for all-solid-state-battery applications. :6.

66. Huo H, Luo J, Thangadurai V, Guo X, Nan C-W, Sun X. Li $_2$ CO $_3$: A Critical Issue for Developing Solid Garnet Batteries. *ACS Energy Lett*. 2020;5(1):252-262. doi:10.1021/acsenergylett.9b02401

67. Tsubokawa N, Kogure A. Surface grafting of polymers onto inorganic ultrafine particles: Reaction of functional polymers with acid anhydride groups introduced onto inorganic ultrafine particles. *J Polym Sci Part Polym Chem*. 1991;29(5):697-702. doi:10.1002/pola.1991.080290511

68. Gupta A, Sakamoto J. Controlling Ionic Transport through the PEO-LiTFSI/LLZTO Interface. *Electrochem Soc Interface*. 2019;28(2):63-69. doi:10.1149/2.F06192if

69. Cheng L, Crumlin EJ, Chen W, et al. The origin of high electrolyte–electrode interfacial resistances in lithium cells containing garnet type solid electrolytes. *Phys Chem Chem Phys*. 2014;16(34):18294-18300. doi:10.1039/C4CP02921F

70. Stolwijk NA, Heddier C, Reschke M, Wiencierz M, Bokeloh J. Salt-Concentration Dependence of the Glass Transition Temperature in PEO–NaI and PEO–LiTFSI Polymer Electrolytes. *Macromolecules*. 2013;46(21):8580-8588. doi:10.1021/ma401686r

71. Whba RAG, TianKhoon L, Su'ait MS, Rahman MYA, Ahmad A. Influence of binary lithium salts on 49% poly(methyl methacrylate) grafted natural rubber based solid polymer electrolytes. *Arab J Chem*. 2020;13(1):3351-3361. doi:10.1016/j.arabjc.2018.11.009

72. Maurel A, Armand M, Grugeon S, et al. Poly(Ethylene Oxide)−LiTFSI Solid Polymer Electrolyte Filaments for Fused Deposition Modeling Three-Dimensional Printing. *J Electrochem Soc*. 2020;167(7):070536. doi:10.1149/1945-7111/ab7c38

73. Fox TG, Flory PJ. Second-Order Transition Temperatures and Related Properties of Polystyrene. I. Influence of Molecular Weight. *J Appl Phys*. 1950;21(6):581-591. doi:10.1063/1.1699711

74. by R. B. Beevers and E. F. T. White. PHYSICAL PROPERTIES OF VINYL POLYMERS. Published online October 19, 1959.

75. L. Eskandarian. *Development and Optimization of Solid Polymer Electrolyte for Lithium Ion Batteries*. Vol PhD Thesis. The University of Western Ontario; 2016.

76. Okubo M, Tanaka Y, Zhou H, Kudo T, Honma I. Determination of activation energy for Li ion diffusion in electrodes. *J Phys Chem B*. 2009;113(9):2840-2847. doi:10.1021/jp8099576

77. X. Zhang, J. Fergus. Solid electrolytes for lithium batteries. *IJTech*. 2018;(6):1178-1186.

78. Al-Salih H. A Polymer-Rich Quaternary Composite Solid Electrolyte for Lithium Batteries. *J Electrochem Soc*. Published online 2020:10.